行政院國家科學委員會專題研究計畫 期末報告

以性別特異性神經保護策略治療出血性腦損傷 - 整合分子與治療解決臨床疾病 (GM03)--以性別特異性神經保護策略治療出血性腦損傷 - 整合分子與治療解決臨床疾病 (GM03)

計 畫 類 別 ： 整合型
計 畫 編 號 ： NSC 101-2629-B-037-001-
執 行 期 間 ： 101 年 08 月 01 日至 102 年 07 月 31 日
執 行 單 位 ： 高雄醫學大學醫學系生理學科

計 畫 主 持 人 ： 許勤
共 同 主 持 人 ： 陳素惠、林志隆、王麗芳、李文森
計畫參與人員： 碩士級-專任助理人員：蕭琇文
學士級-專任助理人員：林萱雅

報 告 附 件 ： 出席國際會議研究心得報告及發表論文

公 開 資 訊 ： 本計畫涉及專利或其他智慧財產權，1 年後可公開查詢

中 華 民 國 102 年 10 月 21 日

中 文 摘 要 ： 顱內出血後經常伴隨著產生過量亞鐵，形成游離基，及誘發存活蛋白如血氧基質酶(HO-1)的表現。然而，HO-1 在腦損傷時扮演的角色仍有爭議。顱內出血後男性存活率較停經前婦女為差。採用檸檬酸亞鐵注射於小鼠尾狀核模擬顱內出血動物模式中，雄鼠尾狀核受損程度亦高於雌鼠。因此，我們採用 HO-1(+/-)基因剔除小鼠來探討 HO-1 在檸檬酸亞鐵引起性別差異性尾狀核損傷所扮演的角色。以 alpha II-spectrin 裂解成 SBDP 145/150 當做損傷嚴重度的指標。並以 TUNEL 染色及 BECN1 免疫染色呈陽性反應者來定義細胞自噬性細胞死亡。結果顯示，檸檬酸亞鐵誘發的 HO-1 表現，損傷嚴重度，及行為缺失，雄鼠皆高於雌鼠。而雌二醇可能是檸檬酸亞鐵引起尾狀核 HO-1 表現及損傷具性別差異性之原因。在雄鼠 HO-1(+/-)組，檸檬酸亞鐵誘發的 DNA 斷裂，損傷嚴重度，及行為缺失皆低於 HO-1(+/+)組。而且，雌二醇對於雄鼠尾狀核免於檸檬酸亞鐵所導致腦損傷的保護作用 HO-1(+/-)組較 HO-1(+/+)組為明顯。比較雌鼠 HO-1(+/-)組與 HO-1(+/-)組，無論是損傷嚴重度或雌二醇的神經保護作用，皆無顯著差異。 以上結果顯示， HO-1 在檸檬酸亞鐵引起尾狀核損傷扮演著性別差異性的角色，即雄鼠 HO-1 減少時檸檬酸亞鐵引起的腦損傷嚴重度較為輕微。本研究結果開啟性別特異性治療的前景，臨床上可針對顱內出血導致較嚴重急性鐵離子過度釋放之男性病患，以減少 HO-1 之誘發性做為預防腦損傷嚴重度之策略。

中文關鍵詞： 性別差異性, 血氧基質酶-1, 檸檬酸亞鐵, 尾狀核

英 文 摘 要 ： Intracerebral hemorrhage (ICH) is associated with overproduction of iron, free radical formation, and induction of survival protein such as heme oxygenase-1 (HO-1) in brain tissue. However, the role of HO-1 induction in participating various brain injury remains controversial. Men have worse survival than premenopausal women after ICH.1 In rodent ICH model using ferrous citrate 2 infusion into the caudate nucleus (CN), slao showed a higher degree of injury severity in CN of males than that in females. HO-1 knockout mice were used to study the role of HO-1 in the sex-difference of FC-induced CN injury. The cleavage of alpha II-spectrin into SBDP 145/150 was used as an indicator of injury severity. Autophagic cell death was identified by TUNEL(+) BECN1 immunoreactivity. The results showed that levels of

FC-induced HO-1 expression, injury severity, and behavioral deficit were higher in males than those in females. Estradiol contributes to the sex dimorphism in FC-induced HO-1 expression and injury severity. In male group, the levels of FC-induced DNA fragmentation, injury severity, histological lesion and behavioral deficit in the CN of HO-1(+/-) were significantly lower than those in HO-1(+/+). Moreover, the neuroprotective effect of E2 against the FC-induced CN injury was enhanced in HO-1(+/-) compared with HO-1(+/+) in males, but not in females. These results suggest that HO-1 plays a sex dimorphic role in FC-induced brain injury. Only in males, the decrease of HO-1 exhibits a beneficial effect on the iron-induced striatal injury. These findings open up the prospect for a sex-specific prevention targeting HO-1 inhibition for male patients suffering from acute iron overload caused by ICH.

英文關鍵詞： sex-dimorphism, heme oxygenase-1, ferrous citrate, caudate nucleus

以性別特異性神經保護策略治療出血性腦損傷 – 整合分子與治療解決臨床疾病（GM03）

Sex-specific neuroprotective strategies for hemorrhage-induced brain injury: Integrated molecular and therapeutic approaches of clinical problems

(性別與科技研究計畫**一年期**計畫期末完整報告)
計畫編號： NSC 101-2629-B-037-001-
執行期限：101 年 8 月 1 日至 102 年 7 月 31 日
主持人：許勤 高雄醫學大學 生理學科
e-mail: chinhsu@cc.kmu.edu.tw
計畫參與人員：蕭琇文
高雄醫學大學 生理學科

中文摘要

顱內出血後經常伴隨著產生過量亞鐵，形成游離基，及誘發存活蛋白如血氧基質酶(HO-1)的表現。然而，HO-1 在腦損傷時扮演的角色仍有爭議。顱內出血後男性存活率較停經前婦女為差。採用檸檬酸亞鐵注射於小鼠尾狀核模擬顱內出血動物模式中，雄鼠尾狀核受損程度亦高於雌鼠。因此，我們採用 HO-1(+/-)基因剔除小鼠來探討 HO-1 在檸檬酸亞鐵引起性別差異性尾狀核損傷所扮演的角色。以 alpha II-spectrin 裂解成 SBDP 145/150 當做損傷嚴重度的指標。並以 TUNEL 染色及 BECN1 免疫染色呈陽性反應者來定義細胞自噬性細胞死亡。結果顯示，檸檬酸亞鐵誘發的 HO-1 表現，損傷嚴重度，及行為缺失，雄鼠皆高於雌鼠。而雌二醇可能是檸檬酸亞鐵引起尾狀核 HO-1 表現及損傷具性別差異性之原因。在雄鼠 HO-1(+/-)組，檸檬酸亞鐵誘發的 DNA 斷裂，損傷嚴重度，及行為缺失皆低於 HO-1(+/+)組。而且，雌二醇對於雄鼠尾狀核免於檸檬酸亞鐵所導致腦損傷的保護作用 HO-1(+/-)組較 HO-1(+/+)組為明顯。比較雌鼠 HO-1(+/-)組與 HO-1(+/-)組，無論是損傷嚴重度或雌二醇的神經保護作用，皆無顯著差異。 以上結果顯示， HO-1 在檸檬酸亞鐵引起尾狀核損傷扮演著性別差異性的角色，即雄鼠 HO-1 減少時檸檬酸亞鐵引起的腦損傷嚴重度較為輕微。本研究結果開啟性別特異性治療的前景，臨床上可針對顱內出血導致較嚴重急性鐵離子過度釋放之男性病患，以減少 HO-1 之誘發性做為預防腦損傷嚴重度之策略。

關鍵字: 性別差異性, 血氧基質酶-1, 檸檬酸亞鐵, 尾狀核

Abstract

Intracerebral hemorrhage (ICH) is associated with overproduction of iron, free radical formation, and induction of survival protein such as heme oxygenase-1 (HO-1) in brain tissue. However, the role of HO-1 induction in participating various brain injury remains controversial. Men have worse survival than premenopausal women after ICH.[1] In rodent ICH model using ferrous citrate [2] infusion into the caudate nucleus (CN), slao showed a higher degree of injury severity in CN of males than that in females. HO-1 knockout mice were used to study the role of HO-1 in the sex-difference of FC-induced CN injury. The cleavage of alpha II-spectrin into SBDP 145/150 was used as an indicator of injury severity. Autophagic cell death was identified by TUNEL(+) BECN1 immunoreactivity. The results showed that levels of FC-induced HO-1 expression, injury severity, and behavioral deficit were higher in males than those in females. Estradiol contributes to the sex dimorphism in FC-induced HO-1 expression and injury severity. In male group, the levels of FC-induced DNA fragmentation, injury severity, histological

lesion and behavioral deficit in the CN of HO-1(+/-) were significantly lower than those in HO-1(+/+). Moreover, the neuroprotective effect of E2 against the FC-induced CN injury was enhanced in HO-1(+/-) compared with HO-1(+/+) in males, but not in females. These results suggest that HO-1 plays a sex dimorphic role in FC-induced brain injury. Only in males, the decrease of HO-1 exhibits a beneficial effect on the iron-induced striatal injury. These findings open up the prospect for a sex-specific prevention targeting HO-1 inhibition for male patients suffering from acute iron overload caused by ICH.

Key words: sex-dimorphism, heme oxygenase-1, ferrous citrate, caudate nucleus

二、緣由與目的

Intracerebral hemorrhage (ICH) is the second most common subtype of stroke and accounts for approximately 10 % to 20 % of all strokes.[1] It has the highest mortality in all stroke types and has a higher rates of stroke incidence and mortality in men than in younger women.[2] It suggests that a greater therapeutic effort should be emphasized in male patients suffered from neurodegeneration after hemorrhagic stroke. Previous studies have indicated that men and women response differently to stroke treatment.[3-4] However, the recommendation for treatment after hemorrhagic stroke appears to be the same in men and women. Thus, understanding the sex dimorphism in host response to stroke insult may help to developing the gender specific preventive and therapeutic strategies for those who suffered from brain functional deficit due to hemorrhagic stroke.

After hemorrhage, blood leaks into brain parenchyma and the heme derived ferrous iron exacerbates intracellular oxidative stress and cellular injury by free radical generation.[5] At the mean time, oxidative stress induces the expression of endogenous survival proteins, such as HO-1.[6] Usually, oxidative stress challenges the induction of HO-1 and subsequently increases the heme catabolism into biliverdin and bilirubin, which is a potent antioxidant.[7] Accordingly, induction of HO-1 may protect cells by argumenting the breakdown of prooxidant heme to the radical scavenging bilirubin.[8] Whereas, in certain experimental conditions, the induction of HO-1 may actually promote rather than protect against cellular injury. A previous report indicated that HO-1 induction was associated with a deleterious iron accumulation in activated microglia in a rodent stroke model.[9] Induction of HO-1 also had a deleterious effect in model of quinolinic acid-induced neurotoxicity, which is probably linked to a hyperproduction of ROS and iron accumulation, and enhanced tissue loss and microglia activation.[10] Therefore, the beneficial or harmful role of HO-1 in brain injury remains controversial and whether a sex dimorphism exists in HO-1 induction after hemorrhagic stroke remains unknown. The present study was designed to test the hypothesis that **HO-1 suppression protects CN from iron-induced injury in a sex dependent manner.**

三、結果與討論

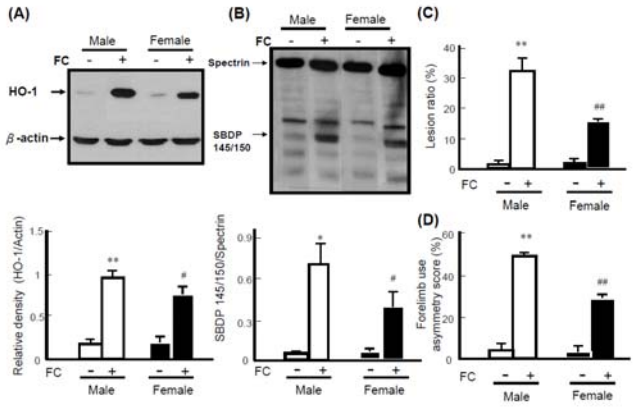

Fig. 1. FC induced higher levels of HO-1 expression and injury severity in CN of intact male mice than that of intact females. (A) Protein level of FC-induced HO-1. Three μL ferrous citrate (FC; 2.55 μmol/L) was infused into the right caudate nucleus (CN). Two days after FC infusion, the brain tissue containing CN was sampled for Western blot analysis. β-actin was used as a sample loading control. **(B) Protein levels of FC-induced cleavage of spectrin.** The levels of spectrin breakdown products 145/150 (SBDP 145/150) in the CN of male and female mice with or without infusion of FC are shown as a ratio of SBDP 145/150 to spectrin acting as an index of severity of injury. **(C) The FC-induced lesion ratio.** The hemispheric area of the CN was quantified according to the density of the hematoxylin and eosin-stained tissue section by Image-pro plus software. The lesion ratio was estimated by dividing the hemispheric volume of the CN on the ipsilateral side by that on the contralateral side. **(D) The FC-induced behavioral deficit.** Forelimb use asymmetry ratio depicting an index of behavioral deficit. Data are expressed as means ± SD (n=6), *P < 0.05, **P < 0.01 compared with sex-matched control. ##<0.01 compared with FC-infusion male group.

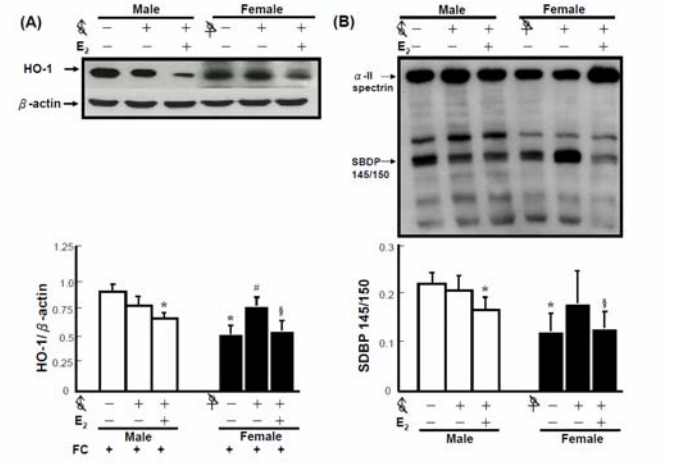

Fig. 2. E_2 contributes to the sex difference of HO-1 induction and injury severity caused by FC-infusion. (A) Effects of castration and E2 implantation on the protein level of HO-1 in male and female mice. Castration was performed 2 weeks before FC-infusion. Silastic tube containing E_2 was implanted one day before FC-infusion. Three μL FC (2.55 μmol/L) was infused into the right CN. Two days after FC infusion, the brain tissue containing CN was sampled. **(B) Effects of castration and E_2 implantation on the severity of FC-induced injury in the CN of male and female mice.** ♂ with a slash indicated castrated male; ♀ with a slash indicates ovariectomized female. The levels of HO-1 and the cleavage of alpha-II spectrin were analyzed by Western blot analysis using antibody for HO-1 and spectrin, respectively. Beta-actin was used as a sample loading control. The representative data of Western blot is shown in the upper panel of the lower quantitative result. Data are expressed as means ± SD (n=6), * p<0.05 compare to intact male; # p<0.05 compare to intact female; §<0.05 compare to ovariectomized female.

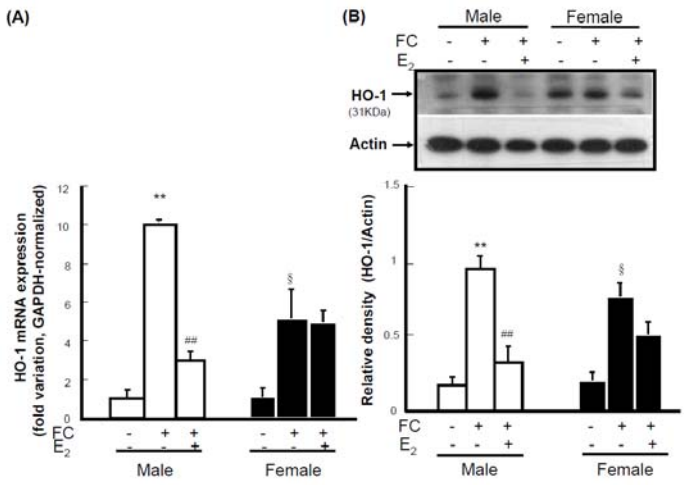

Fig. 3. Exogenous E_2 suppresses the FC-induced HO-1 expression in castrated male mice at both mRNA and protein levels. (A) mRNA levels of FC-induced HO-1. (B) Protein levels of FC-induced HO-1. Castration was performed two weeks before subcutaneous implantation with a silastic tube containing 17β- estradiol benzoate (E_2) at 24 hours before the infusion of FC (3 μL, 2.55 μmol/L). The tissues containing CN were sampled 2 days after infusion of FC for detecting the levels of HO-1 mRNA and protein. FC induced higher levels of mRNA and protein of HO-1 in males than that in females. E_2 suppressed the FC-induced HO-1 expression particularly in males. Data are expressed as means± SD (N=6). **p<0.01 compared with saline-infusion; ##p<0.01 compared with FC-infusion without E2-treated male group; §p<0.05 compared with FC-infusion male group.

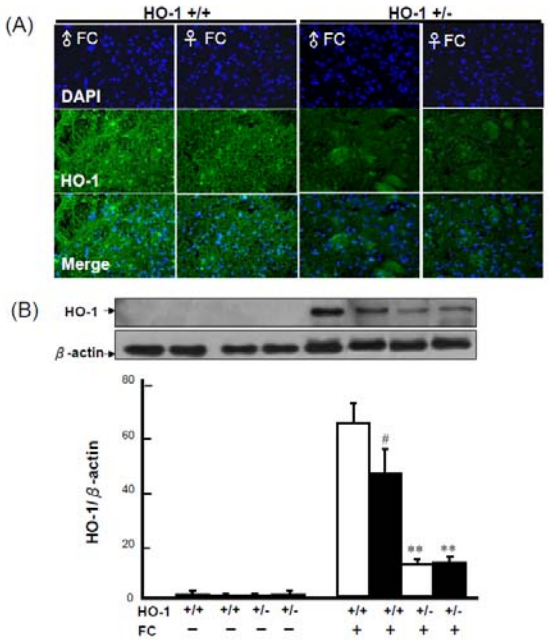

Figure 4. The immunoreactivity and protein level of HO-1 in male and female mice with or without heterozygote knockout of HO-1 gene. (A) HO-1 immunoreactivity. (B) Protein level of HO-1. Because HO-1 (-/-) mice are neonatal lethal, heterozygous HO-1(+/-) male and female mice were used in this study. Three μL FC (2.55 μmol/L) was infused into the right caudate nucleus. Two days after ferrous citrate infusion, the brain tissue containing caudate nucleus was sampled. HO-1 knockout decreased the HO-1 immunoreactivity and HO-1 protein levels in CN of both male and female mice. Data are expressed as means ± SD (n=6). **p<0.01 compared with sex-matched HO-1(+/+) FC-infusion group; #p<0.05, ##p<0.01 compared with HO-1(+/+) FC-infusion male group.

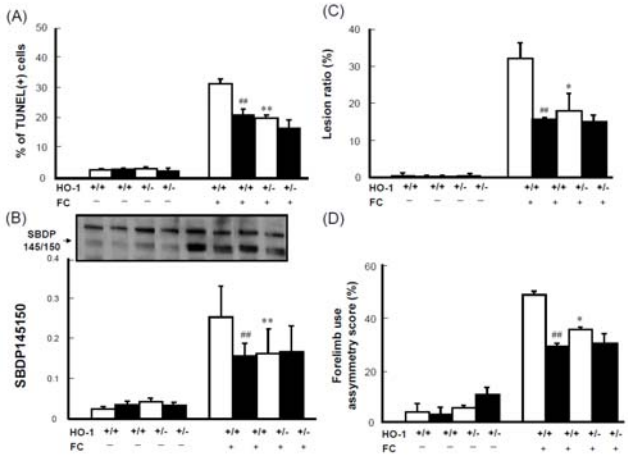

Figure 5. FC-induced CN injury in HO-1(+/-) male mice is lower than that in HO-1(+/+) male mice. (A) FC-induced DNA fragmentation in CN. TUNEL detection kit was used to identify the DNA fragmentation and the percentage of TUNEL(+) cells was quantified after staining. In FC-infusion male groups, the percentage of TUNEL(+) cells in HO-1(+/-) groups was lower than that in HO-1(+/+). **(B) Level of the FC-induced cleavage of α-II spectrin. (C) FC-induced histological lesion in CN. (D) FC-induced behavioral deficit.** Data are expressed as means ± SD (n=6). **p<0.01 compared with sex-matched HO-1(+/+) FC-infusion group; #p<0.05, ##p<0.01 compared with HO-1(+/+) FC-infusion male group.

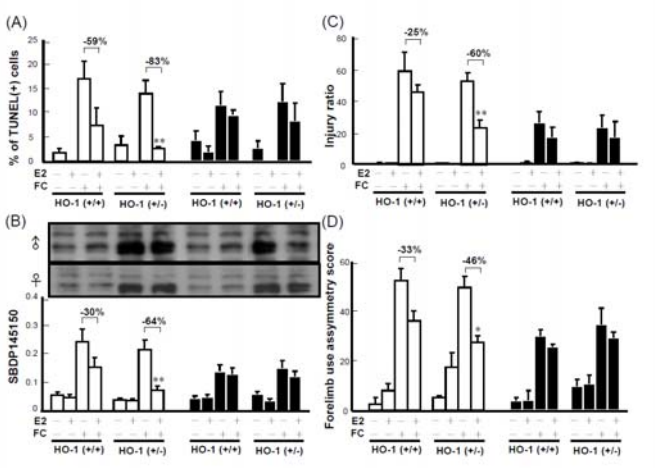

Fig. 6. Sex-dimorphic effect of HO-1 knockout (heterozygote) on the neuroprotection by E_2 against FC-induced CN injury. (A) FC-induced DNA fragmentation in CN. Castration was performed 2 weeks before FC-infusion. Silastic tube containing E_2 was implanted one day before FC-infusion. Three μL FC (2.55 μmol/L) was infused into the right CN. Two days after FC-infusion, the brain tissue containing CN was sampled and sectioned in 5 μm thickness. TUNEL detection kit was used to identify the DNA fragmentation and the percentage of TUNEL(+) cells was quantified after staining. In E_2-pretreated FC-infusion male, the percentage of TUNEL(+) cells in HO-1(+/-) male mice is lower than that in HO-1(+/+) males. **(B) Level of the FC-induced cleavage of α-II spectrin.** The detection of the cleavage of alpha-II spectrin breakdown products (SBDP 145/150) fragment was estimated as a biochemical marker for brain injury. In E_2-pretreated FC-infusion male, the ratio of SBDP 145/150 to spectrin in HO-1(+/-) male mice is lower than that in HO-1(+/+) males. **(C) FC-induced histological lesion in CN.** The hemispheric area of the CN was quantified according to the density of the hematoxylin and eosin-stained tissue section by Image-pro plus software. The lesion ratio was estimated by dividing the hemispheric volume of the CN on the ipsilateral side by that on the contralateral side. In E_2-pretreated FC-infusion male, the lesion ratio in CN of HO-1(+/-) male mice is lower than that in HO-1(+/+) males. **(D) FC-induced behavioral deficit.** Forelimb use asymmetry score depicting an index of

behavioral deficit. H In E_2-pretreated FC-infusion male, FC-induced behavioral deficit in HO-1(+/-) male mice is lower than that in HO-1(+/+) males. Data are expressed as means ± SD (n=6). *p<0.05; **p<0.01 compared with E2-pretreated FC-infusion male group.

結果與討論:

The present study demonstrated that male showed higher levels of FC-induced HO-1 expression, injury severity, and histological lesion associated with behavioral deficit than females in the FC-infusion mouse model, which simulates ICH-induced striatal injury. Heterozygote HO-1 knockout diminished the FC-induced striatal injury in male but not in females. In addition, HO-1 knockout slightly simulates and enhances the neuroprotective effect of E_2. In females, there is no significant effect of HO-1 knockout on FC-induced CN injury or the neuroprotective effect of E_2 on FC-induced CN injury. These results suggest that high level of FC-induced HO-1 in males may exaggerate the FC-induced CN injury, therefore, HO-1 suppression diminished the FC-induced striatal injury and favored the outcome of males. Our study for the first time explored the sex dimorphic effect of HO-1 suppression on the FC-induced striatal injury. These findings open up the prospect for a male-specific prevention targeting HO-1 suppression for patients suffering from striatal iron overload.

Higher levels of FC-induced HO-1 expression and injury severity in CN of male mice than that in females

The ho-1 gene is exquisitely sensitive to induction by a wide range of pro-oxidant and other stressors. Experiments have indicated that, after hemorrhage, clot lysis and iron play an important role in ICH-induced brain injury.[15] Brain iron accumulation may induce neuronal damage even after it has become bound to ferritin because iron can be released in its ferrous form under the acidic conditions.[16] Iron toxicity is largely based on Fenton chemistry where iron reacts with reactive oxygen intermediates to produce highly reactive free radical species such as the hydroxyl radical (OH-).[17] In the present study, a significant higher level of FC-induced HO-1 expression in CN of intact male than that in intact females was observed (Fig. 1A). The endogenous female sex hormones may contribute to the sex difference in HO-1 induction by FC. To delineate whether estradiol participates in the sex difference in HO-1 induction by FC, the effects of exogenous E_2 implantation on HO-1 induction in castrated male and female mice were compared. The result indicated that ovariectomy enhances, while E_2 implantation inhibits the HO-1 induction by FC (Fig. 2A). Accordingly, the suppressive effect of E_2 on HO-1 induction by FC may contribute to the sex differences in CN injury severity caused by FC-infusion.

E_2 may suppress HO-1 induction via an ERα-independent pathway

HO-1 is markedly upregulated in the brain after ICH.[18] The HO-1 gene expression is controlled by the transcriptional activator nuclear factor erythroid 2-related factor 2 (Nrf2) and the

transcriptional repressor breast cancer type 1 susceptibility protein (BRCA1) associated C-terminal helicase1 (Bach-1).[19-20]

After blood infusion in the rat model of ICH, Keap1 showed decreased expression starting at 8 h, whereas Nrf2 began to show a significant increase at 2 h with a peak at 24 h.[21] However, the effect/mechanism of E_2 on HO-1 induction remains controversial. Previous report indicated that E_2 treatment led to Nrf2 dissociation from Keap1 in the cytoplasm, and increased the protein level of Nrf2 in the nucleus, with a significant increase in HO-1 expression homocysteine-treated cells.[22] Another study demonstrated that the protective effects of E2 in male rats were ERα-independent and might be associated with HO-1 inhibition.[23] In the present result, E_2 significantly inhibits HO-1 induction by FC in the CN of male mice at both levels of mRNA and protein, while E_2 inhibits the FC-induced HO-1 expression at the level of protein but not at mRNA level in females (Fig. 3). Since the expression level of ERα mRNA and protein and the number of ERα immunoreactive cells in the CN were higher in female and male brain,[24] the present result indicates an ERα-independent mechanism underlying the suppression of HO-1 expression by E_2 in the CN of male mice. Whereas, further investigation is needed to understand how E_2 decreases the FC-induced HO-1 expression at protein but not at mRNA level in female mice.

Male-specific effect of HO-1 heterozygote knockout (KO) on diminishing FC-induced injury

HO-1 is an enzyme exhibiting both beneficial and harmful effects, depending on the magnitude and time of expression. Its beneficial effects have been related to a decrease in free heme concentrations and further production of anti-oxidant compounds (biliverdin and bilirubin)[25], while a massive HO-1 activation may cause toxic compound accumulation (biliverdin and Fe^{2+}).[26] In hemorrhagic brain of mice, HO-1 expression is mainly observed in microglia/macrophages and vascular endothelial cells around the hematoma region. Deletion of HO-1 gene results in diminution of hemorrhage-induced brain tissue injury.[27] Notably, HO-1 deletion is also associated with a decreased number of activated microglia/macrophages after intracerebral hemorrhage, suggesting that HO-1 supports activated microglia survival that may exacerbate hemorrhage-associated brain injury.[27-28] HO-1 inhibition by SnPP attenuated edema in hemoglobin-induced model of ICH.[29] HO-1 inhibition by tin-mesoporphyrin IX (SnMP) provided significant protection against neuronal loss in rabbits model of autologous blood injection.[30] SnMP-treatment also reduced edema development following experimental ICH in pigs.[31] However, studies using HO-1 inhibition by metalloporphyrin can't exclude it's antioxidant effect.[32] In the present result, interestingly, HO-1 suppression decreased the FC-induced CN injury in male but not in females implicating a harmful role of massive HO-1 induction in males. While the moderate level of HO-1 induction after FC-infusion in female may help the hormesis under redox microenvironment.

HO-1 partial KO enhances the protective effect of E_2 on FC-induced CN injury in males

Estrogen is both a natural neuroprotectant and a potential therapeutic agent for cerebrovascular disease. Several mechanisms may contribute to the beneficial effect of estrogen on brain injury. Previous report have shown that pretreatment with E_2 attenuates brain edema after ICH in male mice.[33] Moreover, administration of exogenous E_2 in male, but not in female rats, significantly attenuated ICH-induced changes in HO-1 when given 2 hours after hemorrhage.[23]This effect of E_2 in males was ER-α-independent and might be associated with HO-1 inhibition.[23] In the present result, no significant effect of HO-1 knockout on E_2 neuroprotection was observed in female group (Fig. 6). While in male mice, HO-1 knockout per se slightly simulates the protective effect of E_2 on FC-induced CN injury. Moreover, HO-1 knockout further enhances the protective effect of E2 against FC-induced CN injury. Results of Western blot and immunohistochemical analysis indicated that ER-α expression was greater in the CN of females compared with that in males.[24] This result suggests that HO-1 suppression partially mediates neuroprotective effect of E_2 and the protective mechanism of HO-1 suppression may be ERα-independent and may be different from that of E_2.

In conclusion, HO-1 plays a sex dimorphic role in FC-induced brain injury and HO-1 silencing has a sex-specific benefit for iron-induced striatal injury only in males they lack of endogenous protection conferred by estradiol. These findings open up the prospect for a male-specific injury prevention targeting HO-1 inhibition for patients suffering from acute iron overload caused by ICH.

Acknowledgments

This work was supported by research grants from the National Science Council of Taiwan (102-2320-B-037-015 to Dr. Hsu; 101-2629-B-037-001 to Dr. Hsu, Dr. Lin, and Dr. Wang).

References:

1. Feigin VL, Lawes CM, Bennett DA, Barker-Collo SL, Parag V. Worldwide stroke incidence and early case fatality reported in 56 population-based studies: a systematic review. *Lancet Neurol* 2009;8(4):355-69.
2. Lewsey JD, Gillies M, Jhund PS, Chalmers JW, Redpath A, Briggs A, et al. Sex differences in incidence, mortality, and survival in individuals with stroke in Scotland, 1986 to 2005. *Stroke* 2009;40(4):1038-43.
3. Kent DM, Price LL, Ringleb P, Hill MD, Selker HP. Sex-based differences in response to recombinant tissue plasminogen activator in acute ischemic stroke: a pooled analysis of randomized clinical trials. *Stroke* 2005;36(1):62-5.
4. Yuan M, Siegel C, Zeng Z, Li J, Liu F, McCullough LD. Sex differences in the response to activation of the poly (ADP-ribose) polymerase pathway after experimental stroke. *Exp Neurol* 2009;217(1):210-8.
5. Frankel D, Mehindate K, Schipper HM. Role of heme oxygenase-1 in the regulation of manganese superoxide dismutase gene expression in oxidatively-challenged

astroglia. *J Cell Physiol* 2000;185(1):80-6.
6. Immenschuh S, Ramadori G. Gene regulation of heme oxygenase-1 as a therapeutic target. *Biochem Pharmacol* 2000;60(8):1121-8.
7. Stocker R. Antioxidant activities of bile pigments. *Antioxid Redox Signal* 2004;6(5):841-9.
8. Baranano DE, Snyder SH. Neural roles for heme oxygenase: contrasts to nitric oxide synthase. *Proc Natl Acad Sci U S A* 2001;98(20):10996-1002.
9. Justicia C, Ramos-Cabrer P, Hoehn M. MRI detection of secondary damage after stroke: chronic iron accumulation in the thalamus of the rat brain. *Stroke* 2008;39(5):1541-7.
10. Tronel C, Rochefort GY, Arlicot N, Bodard S, Chalon S, Antier D. Oxidative stress is related to the deleterious effects of heme oxygenase-1 in an in vivo neuroinflammatory rat model. *Oxid Med Cell Longev* 2013;2013:264935.
11. Hua Y, Schallert T, Keep RF, Wu J, Hoff JT, Xi G. Behavioral tests after intracerebral hemorrhage in the rat. *Stroke; a journal of cerebral circulation* 2002;33(10):2478-84.
12. Sheng Z, Kawano J, Yanai A, Fujinaga R, Tanaka M, Watanabe Y, et al. Expression of estrogen receptors (alpha, beta) and androgen receptor in serotonin neurons of the rat and mouse dorsal raphe nuclei; sex and species differences. *Neurosci Res* 2004;49(2):185-96.
13. Yu L, Alva A, Su H, Dutt P, Freundt E, Welsh S, et al. Regulation of an ATG7-beclin 1 program of autophagic cell death by caspase-8. *Science* 2004;304(5676):1500-2.
14. Kozakowski N, Bohmig GA, Exner M, Soleiman A, Huttary N, Nagy-Bojarszky K, et al. Monocytes/macrophages in kidney allograft intimal arteritis: no association with markers of humoral rejection or with inferior outcome. *Nephrol Dial Transplant* 2009;24(6):1979-86.
15. Hua Y, Keep RF, Hoff JT, Xi G. Deferoxamine therapy for intracerebral hemorrhage. *Acta Neurochir Suppl* 2008;105:3-6.
16. Bishop GM, Robinson SR. Quantitative analysis of cell death and ferritin expression in response to cortical iron: implications for hypoxia-ischemia and stroke. *Brain Res* 2001;907(1-2):175-87.
17. Gaasch JA, Lockman PR, Geldenhuys WJ, Allen DD, Van der Schyf CJ. Brain iron toxicity: differential responses of astrocytes, neurons, and endothelial cells. *Neurochem Res* 2007;32(7):1196-208.
18. Wu J, Hua Y, Keep RF, Nakamura T, Hoff JT, Xi G. Iron and iron-handling proteins in the brain after intracerebral hemorrhage. *Stroke* 2003;34(12):2964-9.
19. Srisook K, Kim C, Cha YN. Molecular mechanisms involved in enhancing HO-1 expression: de-repression by heme and activation by Nrf2, the "one-two" punch. *Antioxid Redox Signal* 2005;7(11-12):1674-87.
20. Igarashi K, Sun J. The heme-Bach1 pathway in the regulation of oxidative stress response and erythroid differentiation. *Antioxid Redox Signal* 2006;8(1-2):107-18.
21. Shang H, Yang D, Zhang W, Li T, Ren X, Wang X, et al. Time course of

Keap1-Nrf2 pathway expression after experimental intracerebral haemorrhage: correlation with brain oedema and neurological deficit. *Free Radic Res* 2013;47(5):368-75.

22. Chen CS, Tseng YT, Hsu YY, Lo YC. Nrf2-Keap1 antioxidant defense and cell survival signaling are upregulated by 17beta-estradiol in homocysteine-treated dopaminergic SH-SY5Y cells. *Neuroendocrinology* 2013;97(3):232-41.
23. Nakamura T, Hua Y, Keep RF, Park JW, Xi G, Hoff JT. Estrogen therapy for experimental intracerebral hemorrhage in rats. *J Neurosurg* 2005;103(1):97-103.
24. Chen TY, Tsai KL, Lee TY, Chiueh CC, Lee WS, Hsu C. Sex-specific role of thioredoxin in neuroprotection against iron-induced brain injury conferred by estradiol. *Stroke* 2010;41(1):160-5.
25. Gozzelino R, Jeney V, Soares MP. Mechanisms of cell protection by heme oxygenase-1. *Annu Rev Pharmacol Toxicol* 2010;50:323-54.
26. Schipper HM, Song W, Zukor H, Hascalovici JR, Zeligman D. Heme oxygenase-1 and neurodegeneration: expanding frontiers of engagement. *J Neurochem* 2009;110(2):469-85.
27. Wang J, Dore S. Heme oxygenase-1 exacerbates early brain injury after intracerebral haemorrhage. *Brain* 2007;130(Pt 6):1643-52.
28. Ohnishi M, Katsuki H, Unemura K, Izumi Y, Kume T, Takada-Takatori Y, et al. Heme oxygenase-1 contributes to pathology associated with thrombin-induced striatal and cortical injury in organotypic slice culture. *Brain Res* 2010;1347:170-8.
29. Huang FP, Xi G, Keep RF, Hua Y, Nemoianu A, Hoff JT. Brain edema after experimental intracerebral hemorrhage: role of hemoglobin degradation products. *J Neurosurg* 2002;96(2):287-93.
30. Koeppen AH, Dickson AC, Smith J. Heme oxygenase in experimental intracerebral hemorrhage: the benefit of tin-mesoporphyrin. *J Neuropathol Exp Neurol* 2004;63(6):587-97.
31. Wagner KR, Hua Y, de Courten-Myers GM, Broderick JP, Nishimura RN, Lu SY, et al. Tin-mesoporphyrin, a potent heme oxygenase inhibitor, for treatment of intracerebral hemorrhage: in vivo and in vitro studies. *Cell Mol Biol (Noisy-le-grand)* 2000;46(3):597-608.
32. Wagner KR, Dwyer BE. Hematoma removal, heme, and heme oxygenase following hemorrhagic stroke. *Ann N Y Acad Sci* 2004;1012:237-51.
33. Nakamura T, Xi G, Hua Y, Schallert T, Hoff JT, Keep RF. Intracerebral hemorrhage in mice: model characterization and application for genetically modified mice. *J Cereb Blood Flow Metab* 2004;24(5):487-94.

附件一

行政院國家科學委員會補助專題研究計畫 ■ 期末報告

（計畫名稱）

以性別特異性神經保護策略治療出血性腦損傷 - 整合分子與治療解決臨床疾病（GM03）

Sex-specific neuroprotective strategies for hemorrhage-induced brain injury: Integrated molecular and therapeutic approaches of clinical problems

計畫類別： ■單一整合型計畫**(**性別與科技研究計畫**一年期**計畫期末完整報告**)**

計畫編號：NSC 101-2629-B-037-001-

執行期限：101 年 8 月 1 日至 102 年 7 月 31 日

計畫主持人：許勤

共同主持人： 李文森、王麗芳、陳素惠、林志隆

計畫參與人員： 蔡克勵、蕭琇文

成果報告類型(依經費核定清單規定繳交)：■完整報告

本成果報告包括以下應繳交之附件：

□赴國外出差或研習心得報告一份

□赴大陸地區出差或研習心得報告一份

■出席國際學術會議心得報告及發表之論文各一份

□國際合作研究計畫國外研究報告書一份

處理方式：除產學合作研究計畫、提升產業技術及人才培育研究計畫、列管計畫及下列情形者外，得立即公開查詢

□涉及專利或其他智慧財產權，■一年 □二年後可公開查詢

執行單位：高雄醫學大學

中 華 民 國 102 年 7 月 31 日

Angiopep-conjugated pluronic F127 superparamagnetic iron oxide nanoparticles as a nanotheranostic agent for brain glioma

Guo-Jing Chen[a#], Ying-Zhen Su[a#], Chin Hsu[b], Jyun-Han Ke[a], Yung-Chih Kuo[c], Chiao-Yun Chen[d], and Li-Fang Wang[a]*

[a]Department of Medicinal & Applied Chemistry, College of Life Science; [b]Faculty of Physiology, College of Medicine, Kaohsiung Medical University, Kaohsiung 80708, Taiwan

[c]Department of Chemical Engineering, National Chung Cheng University, Chia-Yi 62102, Taiwan

[d]Department of Medical Imaging, Kaohsiung Medical University Hospital, Kaohsiung 80708, Taiwan

[#]These authors contributed equally to this work.

***Correspondence to: Li-Fang Wang, Professor of Medicinal & Applied Chemistry**

Kaohsiung Medical University

College of Life Science

100 Shih-Chuan 1st Road, Kaohsiung City 807, Taiwan

Tel: 011-886-7-312-1101 ext. 2217

Fax: 011-886-7-312-5339

E-mail: lfwang@kmu.edu.tw

Manuscript submitted to

ABSTRACT

Pluronic® F127-modified water-dispersible poly(acrylic acid)-bound iron oxide nanoparticles (PF127-PAAIO) were prepared to prevent recognition from the reticuloendothelial system. A blood-brain-barrier penetrating peptide, angiopep-2 (ANG), was conjugated to the surface of PF127-PAAIO to produce multifunctional ANG-PF127-PAAIO. The diameter of 186.5 ± 6.8 nm, saturation magnetization of 76 emu/g Fe, and r2 relaxivity of 167.54 $mM^{-1}s^{-1}$ of ANG-PF127-PAAIO implies its potentiality as a magnetic resonance imaging (MRI) contrast agent. ANG-PF127-PAAIO shows negligible cell cytotoxicity and displays better cellular uptake than PF127-PAAIO into U87 cells for 30 min and 2 h incubation. The T2-weighted image enhancement of -88.1 ± 4.7 % of ANG-PF127-PAAIO is greater than that of -28.8 ± 6.6 % of PF127-PAAIO in U87 cells. Using an orthotopic mice tumor model of U87, ANG-PF127-PAAIO shows the higher sensitivity to depict brain tumor on MR images than PF127-PAAIO does.

Keywords*: Magnetic resonance imaging, Poly(acrylic acid)-bound iron oxide nanoparticles,* Pluronic® F127*, Blood-brain barrier, Angiopep-2*

1. Introduction

The brain is tightly segregated from the circulating blood by a unique layer of highly-specialized and differentiated endothelium barrier, blood-brain barrier (BBB). Many pharmaceuticals cannot be efficiently delivered to, or sustained within the brain; hence, they are ineffective in treating brain diseases. Agarwal *et al*. discussed six approaches that can be employed to improve BBB penetration and deliver therapeutics into the brain [1]. Nanotechnology can be used to bypass the BBB, to target specific cells and infiltrate tumor cells, providing pivotal strategies to solve delivery hurdles to the brain.

The primary advantage of a nanoparticle (NP) carrier is it can cross the BBB and entrap the original characteristics of therapeutic drug molecules. In addition, the NP carrier may reduces drug leaching in the brain and decreases peripheral toxicity [2]. An approach to crossing the BBB can be manipulated using Pluronic® polymers, which consist of poly(ethylene oxide)-poly(propylene oxide)-poly(ethylene oxide) blocks, PEO-PPO-PEO. The hydrophobic PPO segments comprise a hydrophobic core as a microenvironment for the incorporation of lipophilic drugs. The hydrophilic PEO corona prevents aggregation, protein adsorption, and recognition by the reticuloendothelial system (RES) [3]. Pluronic polymers have been studied to promote active membrane transport of numerous anticancer drugs because they overcome the multidrug resistance (MDR) effect. The complex mechanism of Pluronic® effects on MDR cells is mainly attributed to inhibiting drug efflux transporters, such as P-glycoprotein (Pgp), multidrug resistance proteins (MRPs), and breast cancer resistance protein (BCRP) [3]. A product of doxorubicin (DOX) loaded in Pluronic® polymers was launched in a clinical trial in 2004 [4]. Pluronic® micelles have been studied to bypass the BBB for drugs delivery to the central nervous system (CNS) since 2003 [5].

Site specific delivery to the brain has also been facilitated using superparamagnetic iron oxide nanoparticles (SPION). Application of the magnetic field was found to enhance the confinement of

SPION in the brain. Chertok *et al.* synthesized SPION for MRI-monitored magnetic targeting to brain tumors [6]. Using the rat model of orthotopic 9L-gliosarcoma *in vivo*, the authors showed a 5-fold increase in imaging analysis of the total glioma when exposed to SPION with the magnetic field over without ($p= 0.005$) and a 3.6-fold enhancement in the target selectivity index of SPION accumulation in glioma over the normal brain ($p= 0.025$). Jia *et al.* investigated the potential of SPION by employing a standard clinical magneto-encephalographic (MEG) system in conjunction with a superconducting quantum interference device (SQUID) [7]. The results indicated SPION generated evident signals and produced the strong magnetic field. Recently, nanoparticle systems consisting of organic or inorganic polymers-coated SPION and a small chlorotoxin (CTX) peptide on the surface have been developed for multifaceted applications [8-12]. All these studies explain the SPION nanoparticle system is a potential approach for targeted drug delivery against brain gliomas.

In this study, a novel nanoparticle system, potentially applicable for the development of new theranostics with increased brain penetration, includes three compartments: a magnetic iron oxide core, a polymer, and a peptide. Our previously-made polyacrylic acid coated iron oxides (PAAIO) were used as a starting material which had a high superparamagnetic property for MRI [13]. An external magnet could be imposed to accelerate sedimentation of SPION at a brain tumor area through the transcytosis mechanism, to bypass the BBB as stated by Agarwal [1]. PF127, one of the Pluronic® polymers, was conjugated on PAAIO to produce PF127-PAAIO as a drug reservoir for therapeutic agents, which enhances BBB penetration via the inhibiting P-glycoprotein efflux pump mechanism [1]. In addition, a high capability for the BBB penetration peptide, Angiopep-2 (ANG), was conjugated on the surface of PF127-PAAIO to produce ANG-PF127-PAAIO via a simple chemical reaction. This brain targeting ligand facilitates the receptor mediated endocytosis mechanism [1].

Brain targeting ligands are well documented, including antibodies, peptides, and small molecules [14]. Several receptors are present on the luminal endothelial plasma membranes, including transferrin

receptor, insulin receptor, and low-density lipoprotein receptor-related protein (LRP) [15]. ANG (TFFYGGSRGKRNNFKTEEY), derived from the Kunitz domain, is a ligand of low density LRP over-expressed in human glioma cells. It is one of the peptides, exhibiting higher transcytosis capacity and parenchymal accumulation than transferrin, lactoferrin, and avidin, and possessing a high BBB penetration capability [16]. A chemical attachment of different molecules to ANG to bypass the brain via transcytosis was developed [17, 18]. ANG1005 is a prodrug combining ANG with 3 molecules of paclitaxel using cleavable ester bonds [18]. Preclinical studies show brain uptake of ANG1005 is ~100-fold greater than paclitaxel, and once in the brain, ANG1005 favorably targets tumor cells and enters by endocytosis using the same receptor mechanism.

Here, a novel multifunctional ANG-PF127-PAAIO consisting of several beneficial factors to cross the BBB is developed. Physicochemical properties, cellular viability, cellular internalization, saturation magnetization and hysteresis, T2-weighted image, and cellular uptake mechanism in U87 cells were thoroughly characterized. An *in vitro* BBB model was constructed to test its penetration ability and an i*n vivo* orthotopic mouse tumor model of U87 was developed to demonstrate the higher sensitive T2-weighted image observed in using ANG-PF127-PAAIO than using PF127-PAAIO. The authors demonstrate the combination of many beneficial mechanisms on the designed SPION should improve BBB penetration and enhance the payload accumulation in the brain.

2. Materials and methods

2.1. Materials

Iron(III) chloride anhydrous, and sodium hydroxide were purchased from TCI (Tokyo, Japan). Poly(acrylic acid) (PAA) was from Acros (Morris Plains, NJ). Fetal bovine serum (FBS) was from Biological Industries (Beit Haemek, Israel). Minimum Essential Medium (MEM) and trypsin-EDTA were from Invitrogen (Carlsbad, CA). 3-(4,5-Dimethyl- thiazol-2yl)-2,5-diphenyl tetrazolium bromide (MTT) was from MP Biomedicals (Eschwege, Germany). All other unstated chemicals were purchased from Sigma-Aldrich (St. Louis, MO), and used without further purification.

2.2. Synthesis of PF127-succinic anhydride adduct (Succ-PF127)

PF127-succinic anhydride (Succ-PF127) was prepared by placing PF127 (504 mg, 0.04 mmol) and succinic anhydride (6 mg, 0.06 mmol) in a one neck flask, which were dried for 30 min at 80^{o}C under vacuum. The reaction temperature was increased to 130^{o}C and the reaction was stirred for 6 h under argon. The crude product was dissolved in 20 mL dichloromethane, and the insoluble material was removed by filtration. The Succ-PF127 was precipitated in cold ether, filtered and dried. The polymer was further dialyzed using a dialysis tube (Spectra, Millipore, MWCO 1000) for 3 days against double deionized (DD) water. The final product was recovered via lyophilization (yield ~ 80%) and stored in a dry box until use.

2.3. Synthesis of PAAIO, PF127-PAAIO and ANG-F127-PAAIO

PAAIO was synthesized according to our previous publication [13]. PF127-PAAIO and ANG-PF127-PAAIO were synthesized via N-(3-dimethyl aminopropyl)-3-ethylcarbodiimide hydrochloride (EDAC) mediated ester formation. Briefly, 15.6 mg of EDAC was added to 100 mL of PAAIO solution (1 mg/mL in DD water) and stirred for one day at room temperature and pH 7.0. Next,

100 mg of PF127 was added into the above solution and further reacted for another one day to yield PF127-PAAIO. Succ-PF127-PAAIO was similarly prepared for PF127-PAAIO instead of using 100 mg of Succ-PF127. ANG-PF127-PAAIO was prepared by adding 7.6 mg of EDAC to 100 mL of Succ-PF127-PAAIO solution (1 mg/mL in DD water) and stirring at room temperature and pH 7.0 for 6 h followed by adding 9.6 mg of ANG to the above solution and reacting overnight. The PF127-PAAIO and ANG-PF127-PAAIO reaction solutions were transferred to a dialysis tube (Spectra, Millipore, MWCO 25000) and dialyzed against DD water for 2 days. The final products were collected by freeze-drying.

2.4. Preparing Rh123- magnetic nanoparticles (MNPs)

PF127-PAAIO/ANG-PF127-PAAIO (100 mg) and EDAC (10 mg) were dissolved in 90 mL of DD water. The solution was stirred for one day. One mg of Rh123 in 10 mL of DD water was added to the solution, and stirred at room temperature for 6 h in the dark. The reaction solution was dialyzed against DD water for 2 days. The resulting products were collected by freeze-drying.

2.5. Characterizations

^{1}H-NMR spectrum was recorded on a Gemini-200 spectrometer (Varian, Palo Alto, CA) using deuterium oxide (D_2O) as a solvent. Fourier transform infrared (FTIR) spectra were obtained on a Perkin-Elmer-2000 spectrometer (Norwalk, CT). Dried samples were pressed with KBr powder into pellets. Sixty-four scans were signal-averaged in the range of 400-4000 cm^{-1} at a resolution of 4 cm^{-1}. Particle sizes of MNPs were measured using a Zetasizer Nano ZS dynamic light scattering (Malvern, Worcestershire, UK). Light scattering measurements were done with a laser of wavelength 633 nm at a 90° scattering angle. The sample concentration was 0.1 mg/mL and temperature was maintained at 25^{o}C. The particle diameter and morphology of MNPs were also visualized by TEM (Jeol JEM-1400, Tokyo, Japan). One drop of the sample solution was deposited on the grid and dried in air at room

temperature. The CNH contents of MNPS were determined using an elemental analyzer (Elementar Vario EL Ⅲ, Germany). The magnetic properties were measured with a magnetic properties measurement system (MPMS) from Quantum Design (MPMS-XL7), which utilizes a SQUID magnetometer at fields ranging from 15 to -15K Oe at 25^{o}C. The iron concentrations were determined using an atomic absorption spectrometer (AAS) positioned at 248 nm (5100 PC, Perkin Elmer). Transversal relaxivities (r2) were generated using a magnetic resonance (MR) spectroscope (Bruker Biospec 70/30 MRI) equipped with a 7 T MR scanner. Different concentrations of MNPs (5 - 30 mg/L) were prepared in DD water. The transversal relaxation times were measured using a standard fast spin echo with the following parameters: TR: 3000 ms; TE: 15-150 ms; FOV: 60×60 mm^2; matrix: 192×192; slice thickness: 1 mm. The T2-weighed images were acquired using a fast gradient echo pulse sequence (TR/TE/flip angle 3000 ms/75 ms/30^{o}).

2.6. Cell culture, cytotoxicity, and cellular uptake

U87 cells (human glioblastoma cell line) were cultivated and maintained in minimum essential medium (MEM), supplemented with 10% FBS and 100 μg/mL penicillin-streptomycin, at 37 °C under 5% CO_2.

2.6.1. Cytotoxicity

U87 cells were seeded in 96-well culture plates (5×10^3/well). The cytotoxicities were evaluated by determining cell viability after 24 h of incubation with various concentrations of MNPs (5-1000 μg/mL). The viable cells was determined by estimating their mitochondrial reductase activity using the tetrazolium-based colorimetric method [19]. The number of active cells was estimated by measuring the absorbance at 540 nm.

2.6.2. Cellular uptake

U87 cells were seeded in 6-well culture plates (2×10^5/well). Rh123-MNPs were added at a concentration of 200 μg /mL and incubated separately for 30 min and 2 h. The culture medium was removed and washed three times with 1 mL of PBS containing 2% FBS. The cells were detached by 1X trypsin and centrifuged at 1500 rpm for 5 min. The media was removed and resuspended in 1 mL of PBS. Cell accounts of 1×10^4 were immediately analyzed using an EPICS XL flow cytometer (Beckman Coulter, Fullerton, CA).

The cells were also preincubated with different chemical inhibitors, chlorpromazine (10 μg/mL), wortmannin (50 nM), genistein (200 nM), and Mβ-cyclodextrin (1 mM) for 30 min to study the internalization mechanism of the MNPs. The medium containing the inhibitors was changed to fresh MEM, and the cells containing 200 μg /mL Rh123-MNPs were treated and incubated for another 2 h. Next, the cells were trypsinized, centrifuged, and resuspended in 1 mL of PBS and 1×10^4 cell counts were immediately analyzed.

The cellular uptake of MNPs was also quantified using AAS, where 2×10^4 cell counts from each sample were analyzed for iron content. The centrifuged cell pellets were dissolved in 37% HCl at 70^{o}C and let sit for 1 h. The AAS samples were diluted to a volume of 3 mL with DD water for analysis. The iron contents of samples were calculated based on a calibration curve of $FeCl_3$.

2.6.3. Confocal

U87 cells (2×10^5/well) were seeded into a 12-well culture plate in MEM containing one glass coverslip/well and incubated for 24 h at 37 °C. The medium was removed and 1 mL of 100 μg/mL MEM containing Rh123-MNPs was added into each well, followed by incubation at 37 °C for various time periods. The coverslips with cells were treated with 1 mL of 3.7% formaldehyde in 0.1 mL PBS. The cells were treated with 1 mL/well of Triton X-100 and incubated for 10 min. After three PBS

washings, the cells were incubated with 0.5 mL/well of DAPI for 10 min at 37 °C. An Olympus Fv 500 confocal laser scanning microscope (CLSM, Tokyo, Japan) was used for cell imaging. The emission wavelength was set at 565 nm.

2.7. In vitro MRI

The MR spectroscope (Bruker Biospec 70/30 MRI) equipped with the 7 T MR scanner was also used to measure T_2-weighted signal intensities using iron concentrations ranging of 0-30 μg/mL in MEM medium. U87 cells (5×10^5/well) were seeded into a 6-well culture plate 1 d before adding the various concentrations of MNPs. The addition of the samples was followed by incubation for 3 h at 37 °C. The medium was dispensed and the cells were washed three times with 0.1 M PBS containing 2% FBS. The T_2-weighed images were acquired using a fast gradient echo pulse sequence (TR/TE/flip angle 3000 ms/75 ms/30^o).

The enhancement of MR images of the cells after incubated with MNPs *in vitro* is defined by the following equation [20],

2.8. Permeability across cocultured HBMEC/HA system

The permeability across BBB was tested with human brain-microvascular endothelial cell (HBMEC, Biocompare; South San Francisco, CA)/human astrocyte (HA, Sciencell; Corte Del Cedro Carlsbad, CA) system according the previous publication [21]. Poly(ethylene terephthalate) (PET) membrane with the cultured HBMEC/HA was fixed between donor and receiver chambers. HBMECs faced the donor chamber. The two chambers were maintained at 37 ^{o}C by circulating water in the external jacket. The donor chamber was filled with 14 mL of fresh culture medium containing Rh123-MNPs with a concentration of 0.25 mg/mL at 150 rpm. The receiver chamber was filled with 14 mL of fresh culture medium at 150 rpm. Fifty μL of the fluid in the receiver chamber were sampled

at different time periods. The samples were analyzed using a microplate fluorescent reader (Synergy HT; BioTek, Winooski, VT) using excitation at 480 nm and emission at 525 nm. The receiver chamber was immediately compensated with 50 μL of fresh culture medium. The permeability coefficient of Rh123-MNPs across HBMECs, P_{HBMECs}, was calculated by

$$P_t = \frac{J}{\Delta C} = V_r \frac{dC}{dt} \frac{1}{C} \qquad (3)$$

where P_e, P_m, J, ΔC, and V_r are respectively to the permeability across PET membrane with HBMECs, the permeability across PET membrane, the mass flux from donor into receiver, the concentration difference between donor and receiver, and the volume of receiver.

2.9. In vivo MRI

After anesthetized by injected Zoletil, we stereotactically injected U87 cells (1×10^5 cells in 3 μL volume) into the brains of nude mice as reported by Yan et al. [22] with a rate of 1μL/min at stereotactic coordinates 0.5 mm forward and 1.5 mm right of the bregmau, and 2.5 mm deep of intraparenchymal. The intracranial tumors were ready for imaging experiments after the inoculation for three weeks. For all animals, MR images were taken prior to and at selected time points after injection of PF127-PAAIO and ANG-PF127-PAAIO. Mice were anesthetized by inhalation of 1.5% isoflurane in 1:2 O_2/N_2. The MNPs of 10 mg Fe/kg were injected intravenously through the tail vein. The MR imaging was performed using 3.0 T MR imager (Sigma, GE Medical systems; Milwaukee,WI) and using an animal coil (3.8-cm Quadrature Volume Coil). All samples were measured by a T2-weighted spin-echo sequence (TR/TE = 2000/60) for imaging MR imaging.

2.10. Statistical Methods

Means, SD, and SE of the data were calculated. Differences between the experimental groups and the control groups were tested using Student's-Newman-Keuls' test, and $P < 0.05$ was considered significant.

3. Results

The ^{1}H-NMR spectrum of Succ-PF127 in DMSO-d_6 shows a broad peak at 3.5 ppm (methylene units of PEO) and a characteristic methyl peak of PPO at 1.12 ppm (Figure S1). Succinic anhydride peaks at 2.63 ppm and its intensity to that of the methyl groups in PPO were measured and used to calculate a degree of succinic anhydride substitution onto PF127, i.e. ~108 mol%, indicating approximately one end of the hydroxyl groups in PF127 was replaced with succinic anhydride.

A water-soluble PAAIO was synthesized via one-pot reaction according to our previous publication [13]. The conjugation reaction between the hydroxyl groups of Succ-PF127 and the carboxylic groups of PAAIO was carried out at equal molar ratios using EDAC as a coupling agent. The further conjugation between the amino groups of ANG and the carboxylic groups of Succ-PF127-PAAIO was also carried out using EDAC as a conjugation agent in aqueous solution (Scheme 1). A characteristic ester bond stretching at 1722 cm^{-1} in Succ-PF127-PAAIO (Figure S2) implies the successful synthesis of Succ-PF127-PAAIO. The characteristic peaks for carboxylate COO^- on PAAIO appear at 1567 and 1406 cm^{-1}, attributable to asymmetric and symmetric C-O stretching, respectively. A broad peak at 3408 cm^{-1} suggests chemisorption of PAA onto iron oxide surfaces. The absorbance peak of Fe-O on PAAIO appearing at 619 cm^{-1} shifts to 589 cm^{-1} in PF127-PAAIO and ANG-PF127-PAAIO. Since the FTIR measurement is insufficient to distinguish ANG signals of ANG-PF127-PAAIO from those of succ-PF127-PAAIO, thus, elemental analysis (EA) was used to measure the N content and quantitatively estimate the ANG content in ANG-PF127-PAAIO (Table 1). The nitrogen content of 0.46 % was obtained in ANG-PF127-PAAIO, but neither in PAAIO or PF127-PAAIO. The ANG content in ANG-PF127-PAAIO is ~2.72 wt%.

The average hydrodynamic diameters of PAAIO, PF127-PAAIO and ANG-PF127-PAAIO are 46.50 ± 1.4 (PDI = 0.27), 127.6 ± 29.1 (PDI = 0.26) and 186.5 ± 6.8 nm (PDI = 0.32), respectively. The modification of PF127 and ANG-PF127 on the surface of PAAIO increases the hydrodynamic diameter.

The zeta-potentials increase from -54.30 ± 0.28 mV for PAAIO to -15.90 ± 2.73 mV for PF127-PAAIO and -24.30 ± 3.46 mV for ANG-PF127-PAAIO.

The TEM images of PF127-PAAIO and ANG-PF127-PAAIO (Figure 1) show the iron oxide nanoparticles were homogeneously dispersed. The iron contents of PAAIO, PF127-PAAIO and ANG-PF127-PAAIO determined by AAS are 38.6 ± 0.9, 18.4 ± 1.0, and 16.0 ± 0.8 wt%, respectively. The PF127 content in PF127-PAAIO is 52.33 wt% and the ANG-PF127 content in ANG-PF127-PAAIO is 59.55 wt%.

Following polymer decoration, the retained magnetic property of MNPs is an important factor for clinical application as targeted contrast agents for MRI. Therefore, the saturation magnetization value (σs) and the transversal relaxivities (r2) of MNPs were determined. The σs values of MNPs were determined using SQUID, and normalized to the iron mass measured by AAS. The σs values are 86, 80, and 76 emu/g Fe for PAAIO, PF127-PAAIO, and ANG-PF127-PAAIO, respectively (Figure 2(A)). The signal contrast enhancement of the T2-weighted MR images of PAAIO, PF127-PAAIO and ANG-PF127-PAAIO in the iron concentration range of 5 - 30 mg/L in DD water is shown in Figure 2(B). Transversal relaxation rates (1/T2) were plotted as a function of iron concentration, and the r2 values obtained from a slope with the best linear regression are 178.70, 173.12 and 167.54 $mM^{-1}s^{-1}$ for PAAIO, PF127-PAAIO and ANG-PF127-PAAIO, respectively.

To examine the acute cytotoxicity, U87 cells were incubated with MNPs in concentrations of 5 - 500 μg/mL for 24 h. The cell viability, determined by MTT assay, shows U87 cells exposed to PAAIO, PF127-PAAIO and ANG-PF127-PAAIO were non-toxic at all test concentrations. The cell viabilities of U87 cells exposed to three nanoparticles are still >90% even at a high concentration of 500 μg/mL (Figure S3).

The cellular uptake of MNPs into U87 cells with and without ANG was tested. Figure 3(A&B) shows a distinguishable right shift in Rh123-ANG-PF127-PAAIO but not in Rh12-PF127-PAAIO, as

compared with the control group at both 30 min and 2 h incubation time. The cellular uptake in U87 cells increases with increasing incubation time from 30 min to 2 h and the MNPs with an angiopep-2 moiety show the higher internalization in U87 cells. To reconfirm ANG-PF127-PAAIO has better localization in U87 cells than PF127-PAAIO; the iron content in the cells was directly stained with Prussian blue. The internalized Fe^{3+} ions of MNPs became bright blue pigments when reacting with the ferrocyanide ions. There is no discernible blue color either in PF127-PAAIO-treated U87 cells after 30 mins or 2 h incubation (Figure 3(C&D)). In contrast, after the cells had been treated with ANG-PF127-PAAIO (Figure 3(E&F)), the blue color was found at 30 mins and became more noticeable at 2 h. The cellular uptake of the nanoparticles in U87 cells was also quantified by measuring the iron content per cell using AAS (Figure 3(G)). The iron contents in U87 cells are 5.2 and 8.1 μg Fe/mg protein for PF127-PAAIO and ANG-PF127-PAAIO after 30 min of incubation, and 6.0 and 10.2 μg Fe/mg protein after 2 h of incubation. Comparing confocal images with Rh123-PF127-PAAIO, Rh123-ANG-PF127-PAAIO shows higher red fluorescence intensity (Figure 4). The red fluorescence was seen in the nucleus as U87 cells had been exposed to Rh123-ANG-PF127-PAAIO for 2 h, implying ANG-PF127-PAAIO could be used as a drug delivery carrier for a hydrophobic anticancer agent for future study. To check whether U87 cells overexpress low density LRP, an Alexa Fluor®-linked LRP antibody was used to test its binding ability. Indeed, it was found the strong green fluorescence appears in the cell surfaces, indicating U87 cells truly overexpress low density LRP. (Figure S4).

Several different metabolic inhibitors were used to check internalization pathways of the nanoparticles entering U87 cells. The U87 cells were exposed to various inhibitors before they were treated with Rh123-MNPs. Three major mechanisms were tested using their corresponding chemical inhibitors: chlorpromazine (CPZ) for clathrin-mediated endocytosis, genistein and methyl-β-cyclodextrin (Mβ-CD) for caveolae-mediated endocytosis, and wortmannin for macropinocytosis. The cytotoxicities of the inhibitors were tested and the inhibitors were found to be

nontoxic to U87 cells at the concentrations used (data not shown). The flow cytometric diagrams clearly shift left when the cells were pretreated with CPZ, and remain intact when the cells were pretreated with genistein, Mβ-CD, and wortmannin before adding the Rh123-MNPs into U87 cells (Figure S5).

Figure 5(A) shows the amount of Rh123-MNPs permeated across the PET membrane with HBMEC/HA system *in vitro* over a time period of 8 h. The permeation amount is 7.6 and 4.9 μg/mL for Rh123-ANG-PF127-PAAIO and Rh123-PF127-PAAIO at 8 h, respectively. Figure 5(B) shows the permeability coefficient (P_{HBMEC}) of ANG-PF127-PAAIO across the membrane is 4.4×10^{-6} cm/s and 2.3×10^{-6} cm/s of PF127-PAAIO. P_{HBMEC} increases with an ANG modification.

The potential of MNPs as a targeted MR contrast agent to cancer cells was determined from the T2-weighted MR phantom images. The enhancement of PF127-PAAIO is trivial (0.46%), while ANG-PF127-PAAIO is significant (-88.14%) at a Fe concentration of 30 μg/mL (Figure 6A). Consistent with the result in cellular uptake studies, the T2-weighted MR phantom images of ANG-PF127-PAAIO shows a profoundly increased negative contrast enhancement.

Tumor-bearing mice were prepared by injecting U87 cells into the brain of mice, and then MR imaging of the mice was performed at 6 h after the intravenous injection of ANG-PF127-PAAIO and PF127-PAAIO in PBS buffer solution (10 mg Fe/kg). The injected tumors were seen at hyperintense areas in the T2-weighted MR images as indicated by arrows (Figure 6(B&C)). Six hours post injection of ANG-PF127-PAAIO, a noticeable darkening appears in the tumor area in the T2-weighted MR image (Figure 6C), indicative of the accumulation of detectable amounts of ANG-PF127-PAAIO within the tumor. However, no visible enhancement was observed post injection of PF127-PAAIO (Figure 6B).

4. Discussion

The increase in polymer contents and particle diameter following modification of PAAIO with PF127 and ANG-PF127 confirmed the successful synthesis of PF127-PAAIO and ANG-PF127-PAAIO. Besides, the increase in zeta-potential value from -54.30 ± 0.28 mV for PAAIO to -15.90 ± 2.73 mV for PF127-PAAIO implied the successful conjugation of PF127 and PAAIO. The carboxylic acid groups on the surface of PAAIO formed ester bonds with the hydroxyl groups of PF127, resulting in decreased negative charge density. The zeta potential of ANG-PF127-PAAIO decreased to -24.30 ± 3.46 mV after PF127-PAAIO had been linked with ANG. This agrees with the literature, where the modification of ANG on a cationic PEG-dendrimer decreased the surface charge from 16.7 mV to 11.6 mV [22]. In addition, the particle size is a factor determining the performance of ANG-PF127-PAAIO for *in vivo* delivery. The particle sizes are preferred to be >10 nm to escape renal clearance and < 200 nm to prevent sequestration from the RES of the spleen and liver [23]. The hydrodynamic diameter of ANG-PF127-PAAIO nanoparticles was 186 ± 6.8 nm, which fell in the size border to prevent sequestration by the RES [24, 25].

To check the MRI contrast enhancement ability of our synthesized MNPs, both σs and r2 values were measured. The decrease in σs value after PAAIO was coated with PF127 or ANG-PF127 was insignificant. The polymer-coated MNPs were still superparamagnetic with negligible hysteresis at room temperature. In addition, the coating of ANG-PF127 or PF127 on PAAIO slightly affected the performance of r2 values. This result agreed with the PEGylated surface of poly(ethylene imine)-Fe_2O_3 nanoparticles, which also induced a slight change in r2 value [26, 27]. The large r2 values of PF127-PAAIO (173.12 $mM^{-1}s^{-1}$) and ANG-PF127-PAAIO (167.54 $mM^{-1}s^{-1}$) implied they could be a good MRI contrast agent, as compared with most of the conventional MNP products, AMI-25 (100 $mM^{-1}s^{-1}$) and AMI-227 (53 $mM^{-1}s^{-1}$) [28].

The Prussian blue and AAS results were consistent with the finding in flow cytometric studies, where ANG-PF127-PAAIO had higher cellular uptake ability than PF127-PAAIO in U87 cells did. This may be attributable to ANG recognition of the low density LRP.

Brain microvascular endothelial cells (BMECs) are the main cellular component of the BBB [29]. When BMECs are prepared on a porous membrane, the monolayer cell resembles the feature of the BBB *in vivo*. A BBB model by HBMECs/HAs via a transwell culture with an insert of PET membrane was established to analyze the potential targeting efficacy. ANG-PF127- PAAIO could be transported across HBMECs/HAs membrane than PF127-PAAIO did. A better BBB permeation effect with a ANG conjugation was reported in ANG-conjugated poly(ethylene glycol)-co-poly(ε-caprolactone) nanoparticles (ANG-PEG-NP), which also showed the better cellular uptake using brain capillary endothelial cells (BCECs) [30]. In a mouse model, a high accumulation of ANG-PEG-NP was observed in the cortical layer, lateral ventricle, third ventricles and hippocampus. The paclitaxel (PTX) encapsulated ANG-PEG-NP showed high ability to transport across the BBB, no acute toxicity to the hematological system, and high inhibitory effects on U87 MG glioma cells [30, 31]. In addition, the ANG-modified 1,2-Distearoyl-sn-glycero-3-phosphoethanolamine-N-[methoxy (polyethylene glycol)-2000] (ANG-PE-PEG) micelles effectively delivered Amphotericin B (AmB) into the central nerve system (CNS) and maintained higher drug concentration than those without ANG in the brain parenchyma [32]. All these promising results were attributed to recognition of the ANG molecule by the low density LRP. Thus, ANG-PF127-PAAIO could potentially deliver hydrophobic drugs to the brain via the same mechanism.

Four chemical pinocytosis pathway inhibitors were tested. Genistein is a specific tyrosine kinase inhibitor that locally disrupts the actin cytoskeleton and prevents recruitment of dynamin II, indispensable for both caveolae-mediated endocytosis and Rho-mediated endocytosis [33, 34]. Wortmannin is a phosphatidyl inositol-3-phosphate inhibitor that inhibits the macropinocytosis pathway [35]. Mβ-CD is known to disrupt the lipid raft structure and inhibit lipid raft clustering in

response to cytokine stimulation by binding to and sequestering cholesterol from the plasma membrane [36]. CPZ, a cationic amphiphilic drug, inhibits clathrin-mediated endocytosis by obstructing the assembly of the clathrin adaptor protein at the cell surface [37]. Compared with the control, the cellular uptake of Rh123-MNPs manifestly decreased when the cells were preincubated with CPZ, indicating clathrin-mediated endocytosis is a primary pathway for internalizing the nanoparticles into the cells. Clathrin inhibition induced an observable decrease in the cellular uptake of Rh123-MNPs. This differs from the report on ANG-PEG-NP, where the caveole-mediated pathway was used [30]. Nevertheless, using the dual-mediated internalization pathway has a high impact on the cellular uptake of nanoparticles [30, 32].

The MRI abilities of the nanoparticles were determined *in vitro* and *in vivo*. The angiopep-2 receptor-mediated endocytosis resulted in a distinguishable darkening of MR images in U87 cells. Because of the high accumulation of ANG-PF127-PAAIO within the tumor as compared with that of PF127-PAAIO *in vivo,* a better negative contrast effect in an orthotopic nude mouse model was obtained. The decrease in signal was sufficient to help a radiologist detect the tumor in the brain. A similar *in vivo* MRI ability was reported in lactoferrin-conjugated SPION (Lf-SPION) as a specific MRI contrast agent for detecting brain glioma [38]. Lactoferrin is also a ligand helping in the transcytosis across the BBB through recognizing the low density LRP [39]. Lf-SPION had greater accumulation in glioma and improved high contrast between the tumor and surrounding normal brain tissue over a period of 48 h. Since the σs and r2 values of ANG-PF127-PAAIO were higher than those of Lf-SPIONs (51 emu/g Fe and 75.6 $mM^{-1}S^{-1}$, respectively), the authors believe ANG-PF127-PAAIO could also be a potent MRI contrast agent for detecting brain glioma.

5. Conclusion

The brain tumor targeting ANG-PF127-PAAIO was successfully synthesized. ANG-PF127-PAAIO retained high levels of superparamagnetic characteristics and MRI ability. ANG-PF127-PAAIO having a BBB penetrating peptide showed a better cellular internalization than PF127-PAAIO in the LRP-overexpressed U87 cells. This result was confirmed by CLSM, flow cytometry, AAS, *in vitro* BBB penetration, and T2 image enhancement studies. ANG-PF127-PAAIO exhibited a strong dual-targeting property, because ANG mediated the transport of ANG-PF127-PAAIO across the BBB through the LRP as the first targeting, followed by endocytosis of ANG-PF127-PAAIO via recognition of the clathrin-mediated receptor on the U87 surfaces as the second targeting. ANG-PF127-PAAIO contains the superparamagnetic Fe_3O_4, the micellar PF127, and a BBB targeting ANG, thus, it has potential to be used as a diagnostic imaging agent as well as a chemotherapeutic agent specifically targeting brain diseases.

Acknowledgements

This paper was supported by the National Science Council of Taiwan under the grant numbers of NSC 100-2320-B037-003-MY3, NSC 101-2325-B037-006, 101-2629-B-037-001 and NSC-102-2325-B037-005.

Appendix A. Supplementary data

Supplementary data related to this article can be found online at

References

[1] Agarwal A, Lariya N, Saraogi G, Dubey N, Agrawal H, Agrawal GP. Nanoparticles as novel carrier for brain delivery: a review. Curr Pharm Des 2009;15:917-25.
[2] Lockman PR, Mumper RJ, Khan MA, Allen DD. Nanoparticle technology for drug delivery across the blood-brain barrier. Drug Dev Ind Pharm 2002;28:1-13.
[3] Batrakova EV, Kabanov AV. Pluronic block copolymers: evolution of drug delivery concept from inert nanocarriers to biological response modifiers. J Control Release 2008;130:98-106.
[4] Danson S, Ferry D, Alakhov V, Margison J, Kerr D, Jowle D, et al. Phase I dose escalation and pharmacokinetic study of pluronic polymer-bound doxorubicin (SP1049C) in patients with advanced cancer. British J Cancer 2004;90:2085-91.
[5] Kabanov AV, Batrakova EV, Miller DW. Pluronic block copolymers as modulators of drug efflux transporter activity in the blood-brain barrier. Adv Drug Del Rev 2003;55:151-64.
[6] Chertok B, Moffat BA, David AE, Yu F, Bergemann C, Ross BD, et al. Iron oxide nanoparticles as a drug delivery vehicle for MRI monitored magnetic targeting of brain tumors. Biomaterials 2008;29:487-96.
[7] Jia W, Xu G, Sclabassi RJ, Zhu JG, Bagic A, Sun M. Detection of magnetic nanoparticles with magnetoencephalography. J Magnetism Magnetic Mater 2008;320:1472-8.
[8] Veiseh O, Sun C, Fang C, Bhattarai N, Gunn J, Kievit F, et al. Specific targeting of brain tumors with an optical/magnetic resonance imaging nanoprobe across the blood-brain barrier. Cancer Res 2009;69:6200-7.
[9] Veiseh O, Gunn JW, Kievit FM, Sun C, Fang C, Lee JS, et al. Inhibition of tumor-cell invasion with chlorotoxin-bound superparamagnetic nanoparticles. Small 2009;5:256-64.
[10] Chen AM, Zhang M, Wei D, Stueber D, Taratula O, Minko T, et al. Co-delivery of Doxorubicin and Bcl-2 siRNA by Mesoporous Silica Nanoparticles Enhances the Efficacy of Chemotherapy in Multidrug-Resistant Cancer Cells. Small 2009;5:2673-7.
[11] Sun C, Veiseh O, Gunn J, Fang C, Hansen S, Lee D, et al. In vivo MRI detection of gliomas by chlorotoxin-conjugated superparamagnetic nanoprobes. Small 2008;4:372-9.
[12] Kohler N, Sun C, Fichtenholtz A, Gunn J, Fang C, Zhang M. Methotrexate-immobilized poly(ethylene glycol) magnetic nanoparticles for MR imaging and drug delivery. Small 2006;2:785-92.
[13] Lin JJ, Chen JS, Huang SJ, Ko JH, Wang YM, Chen TL, et al. Folic acid-Pluronic F127 magnetic nanoparticle clusters for combined targeting, diagnosis, and therapy applications. Biomaterials 2009;30:5114-24.
[14] Gabathuler R. Approaches to transport therapeutic drugs across the blood-brain barrier to treat brain diseases. Neurobiol Dis 2009;37:48-57..
[15] Visser CC, Voorwinden LH, Crommelin DJ, Danhof M, de Boer AG. Characterization and modulation of the transferrin receptor on brain capillary endothelial cells. Pharm Res 2004;21:761-9.
[16] Demeule M, Currie JC, Bertrand Y, Che C, Nguyen T, Regina A, et al. Involvement of the low-density lipoprotein receptor-related protein in the transcytosis of the brain delivery vector Angiopep-2. J Neurochem 2008;106:1534-44.
[17] Thomas FC, Taskar K, Rudraraju V, Goda S, Thorsheim HR, Gaasch JA, et al. Uptake of ANG1005, A Novel Paclitaxel Derivative, Through the Blood-Brain Barrier into Brain and Experimental Brain Metastases of Breast Cancer. Pharm Res 2009;26:2486-94.
[18] Regina A, Demeule M, Che C, Lavallee I, Poirier J, Gabathuler R, et al. Antitumour activity of ANG1005, a conjugate between paclitaxel and the new brain delivery vector Angiopep-2. Br J Pharmacol 2008;155:185-97.
[19] Mosmann T. Rapid Colorimetric Assay for Cellular Growth and Survival - Application to Proliferation and Cyto-Toxicity Assays. J Immunol Methods 1983;65:55-63.

[20] Chen TJ, Cheng TH, Chen CY, Hsu SCN, Cheng TL, Liu GC, et al. Targeted Herceptin-dextran iron oxide nanoparticles for noninvasive imaging of HER2/neu receptors using MRI. J Biol Inorg Chem 2009;14:253-60.
[21] Kuo YC, Yu HW. Transport of saquinavir across human brain-microvascular endothelial cells by poly(lactide-co-glycolide) nanoparticles with surface poly-(gamma-glutamic acid). Int J Pharm 2011;416:365-75.
[22] Yan HH, Wang JY, Yi PW, Lei H, Zhan CY, Xie C, et al. Imaging brain tumor by dendrimer-based optical/paramagnetic nanoprobe across the blood-brain barrier. Chem Commun 2011;47:8130-2.
[23] Shubayev VI, Pisanic TR, 2nd, Jin S. Magnetic nanoparticles for theragnostics. Adv Drug Deliv Rev 2009;61:467-77.
[24] Wang YXJ, Hussain SM, Krestin GP. Superparamagnetic iron oxide contrast agents: physicochemical characteristics and applications in MR imaging. Eur Radiol 2001;11:2319-31.
[25] Hahn PF, Stark DD, Lewis JM, Saini S, Elizondo G, Weissleder R, et al. First clinical trial of a new superparamagnetic iron oxide for use as an oral gastrointestinal contrast agent in MR imaging. Radiology 1990;175:695-700.
[26] Schweiger C, Pietzonka C, Heverhagen J, Kissel T. Novel magnetic iron oxide nanoparticles coated with poly(ethylene imine)-g-poly(ethylene glycol) for potential biomedical application: Synthesis, stability, cytotoxicity and MR imaging. Int J Pharm 2011;408:130-7.
[27] Cai HD, An X, Cui J, Li JC, Wen SH, Li KG, et al. Facile Hydrothermal Synthesis and Surface Functionalization of Polyethyleneimine-Coated Iron Oxide Nanoparticles for Biomedical Applications. Acs Appl Mater Inter 2013;5:1722-31.
[28] Jun YW, Lee JH, Cheon J. Chemical design of nanoparticle probes for high-performance magnetic resonance imaging. Angew Chem Int Edit 2008;47:5122-35.
[29] Andrieux K, Couvreur P. Nanoparticles for brain delivery of drugs or contrast agents. Application to Alzheimer's disease. Biologie aujourd'hui 2012;206:185-90.
[30] Xin HL, Sha XY, Jiang XY, Chen LC, Law K, Gu JJ, et al. The brain targeting mechanism of Angiopep-conjugated poly(ethylene glycol)-co-poly(epsilon-caprolactone) nanoparticles. Biomaterials 2012;33:1673-81.
[31] Xin HL, Jiang XY, Gu JJ, Sha XY, Chen LC, Law K, et al. Angiopep-conjugated poly(ethylene glycol)-co-poly(epsilon-caprolactone) nanoparticles as dual-targeting drug delivery system for brain glioma. Biomaterials 2011;32:4293-305.
[32] Shao K, Wu JQ, Chen ZQ, Huang SX, Li JF, Ye LY, et al. A brain-vectored angiopep-2 based polymeric micelles for the treatment of intracranial fungal infection. Biomaterials 2012;33:6898-907.
[33] Hufnagel H, Hakim P, Lima A, Hollfelder F. Fluid phase endocytosis contributes to transfection of DNA by PEI-25. Mol Ther 2009;17:1411-7.
[34] Parton RG, Joggerst B, Simons K. Regulated internalization of caveolae. J Cell Biol 1994;127:1199-215.
[35] Araki N, Johnson MT, Swanson JA. A role for phosphoinositide 3-kinase in the completion of macropinocytosis and phagocytosis by macrophages. J Cell Biol 1996;135:1249-60.
[36] Lee MY, Ryu JM, Lee SH, Park JH, Han HJ. Lipid rafts play an important role for maintenance of embryonic stem cell self-renewal. J Lipid Res 2010;51:2082-9.
[37] Khalil IA, Kogure K, Akita H, Harashima H. Uptake pathways and subsequent intracellular trafficking in nonviral gene delivery. Pharmacol Rev 2006;58:32-45.
[38] Xing JF, Deng LD, Xie CP, Xiao L, Zhai YL, Jin FM, et al. Methoxy poly(ethylene glycol)-b-poly(octadecanoic anhydride)-b-methoxy poly(ethylene glycol) amphiphilic triblock copolymer nanoparticles as delivery vehicles for paclitaxel. Polym Advan Technol 2011;22:669-74.
[39] Fillebeen C, Descamps L, Dehouck MP, Fenart L, Benaissa M, Spik G, et al. Receptor-mediated transcytosis of lactoferrin through the blood-brain barrier. The J Bio Chem 1999;274:7011-7.

Table 1. The carbon (C), nitrogen (N) and hydrogen (H) content of PAAIO, PF127-PAAIO and ANG-PF127-PAAIO determined by elemental analyzer (EA) (n= 3).

	N%	C%	H%
PAAIO	N.D.	19.21±0.23	4.13±0.25
PF127-PAAIO	N.D.	40.65±0.21	6.93±0.03
ANG-PF127-PAAIO	0.46±0.02	40.30±0.42	6.91±0.01

Figure Captions

Figure 1. Transmission electron microscope (TEM) images of (A) PAAIO; (B) PF127-PAAIO; (C) ANG-PF127-PAAIO.

Figure 2. (A) The magnetization curve as a function of field and (B) T2-weighted magnetic resonance (MR) phantom images for PAAIO, PF127-PAAIO and ANG-PF127-PAAIO.

Figure 3. Flow cytometric diagrams of Rh123-PF127-PAAIO and Rh123-ANG-PF127-PAAIO in U87 cells after (A) 30 min and (B) 2 h of incubation; prussian blue-stained U87 cell after incubation with (C, D) PF127-PAAIO and (E, F) ANG-PF127-PAAIO for (C, E) 30 min and (D, F) 2 h at 37 °C; and (G) the iron content in U87 cells measured by AAS.

Figure 4. CLSM images of U87 cells exposed to (A, B) Rh123-PF127-PAAIO and (C, D) Rh123-ANG-PF127-PAAIO for (A, C) 30 min and (B, D) 2 h at 37 °C.

Figure 5. (A) Permeability concentration and (B) permeability coefficient of PF127-PAAIO and ANG-PF127-PAAIO across HBMEC

Figure 6. (A) *T*2-weighted MR phantom images of U87 cells after incubation with the various concentrations of PF127-PAAIO and ANG-PF127-PAAIO, the MRI brain images of mice with tumor and after 6 h postinjection of 10 mg Fe/Kg of (B) PF127-PAAIO and (C) ANG-PF127-PAAIO via tail vein. The area with the arrow indicates the allograft tumor region.

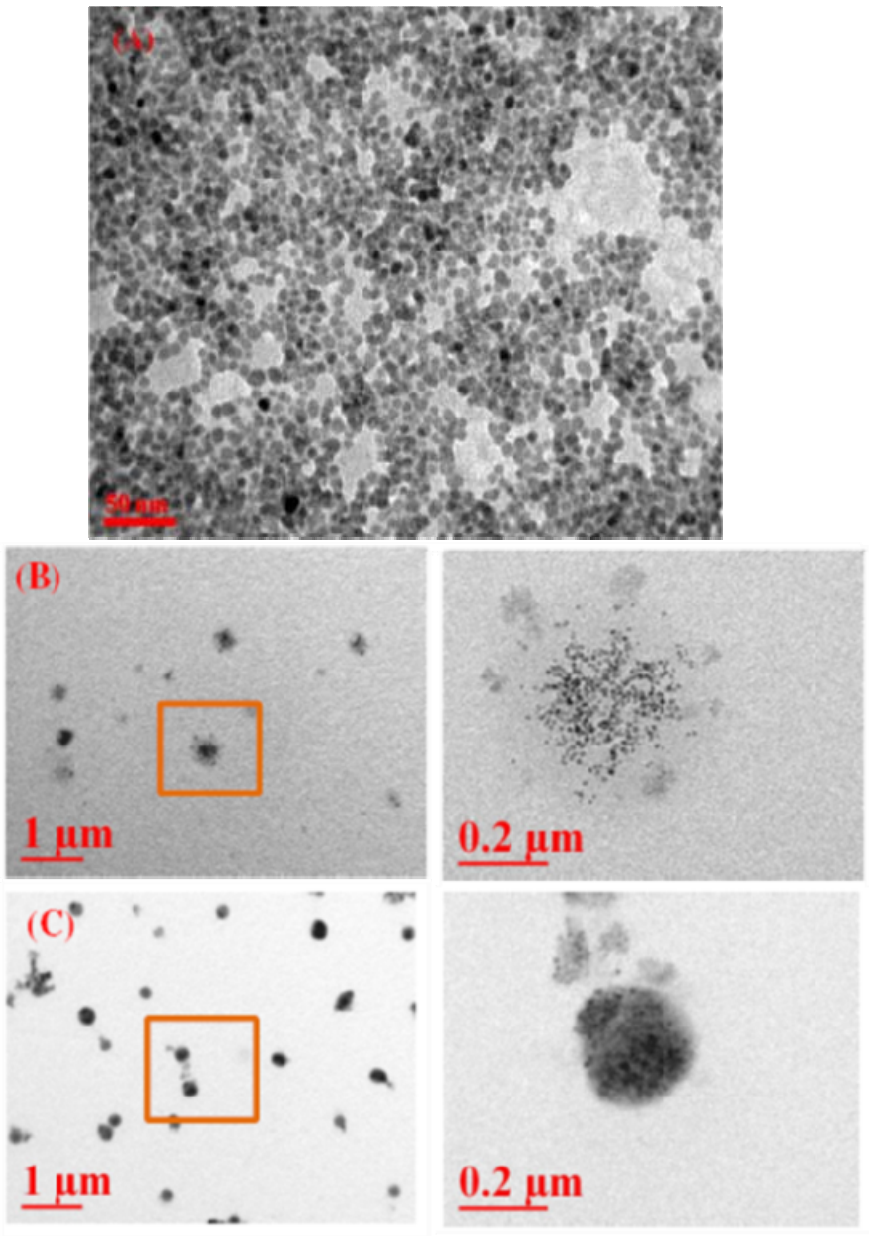

Figure 1.

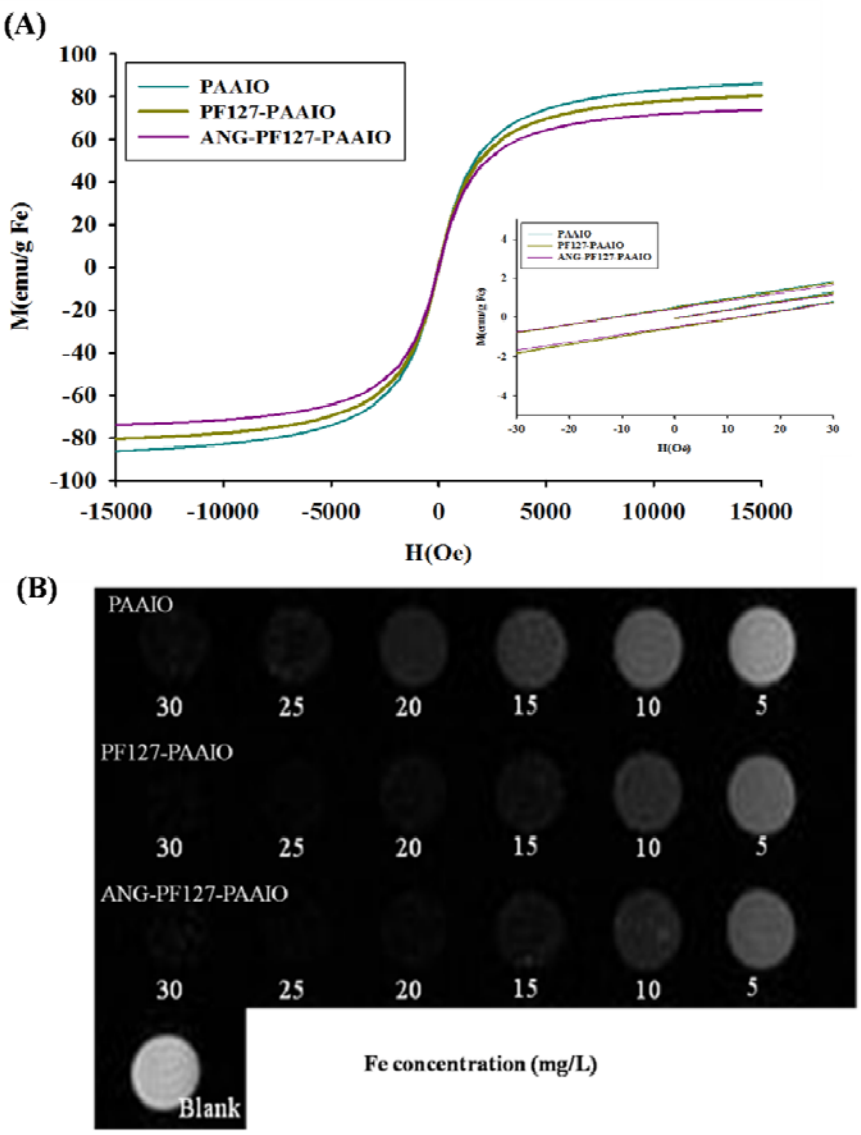
(A)
PAAIO
PF127-PAAIO
ANG-PF127-PAAIO
M(emu/g Fe)
H(Oe)
(B)
PAAIO
30 25 20 15 10 5
PF127-PAAIO
30 25 20 15 10 5
ANG-PF127-PAAIO
30 25 20 15 10 5
Blank
Fe concentration (mg/L)

Figure 2.

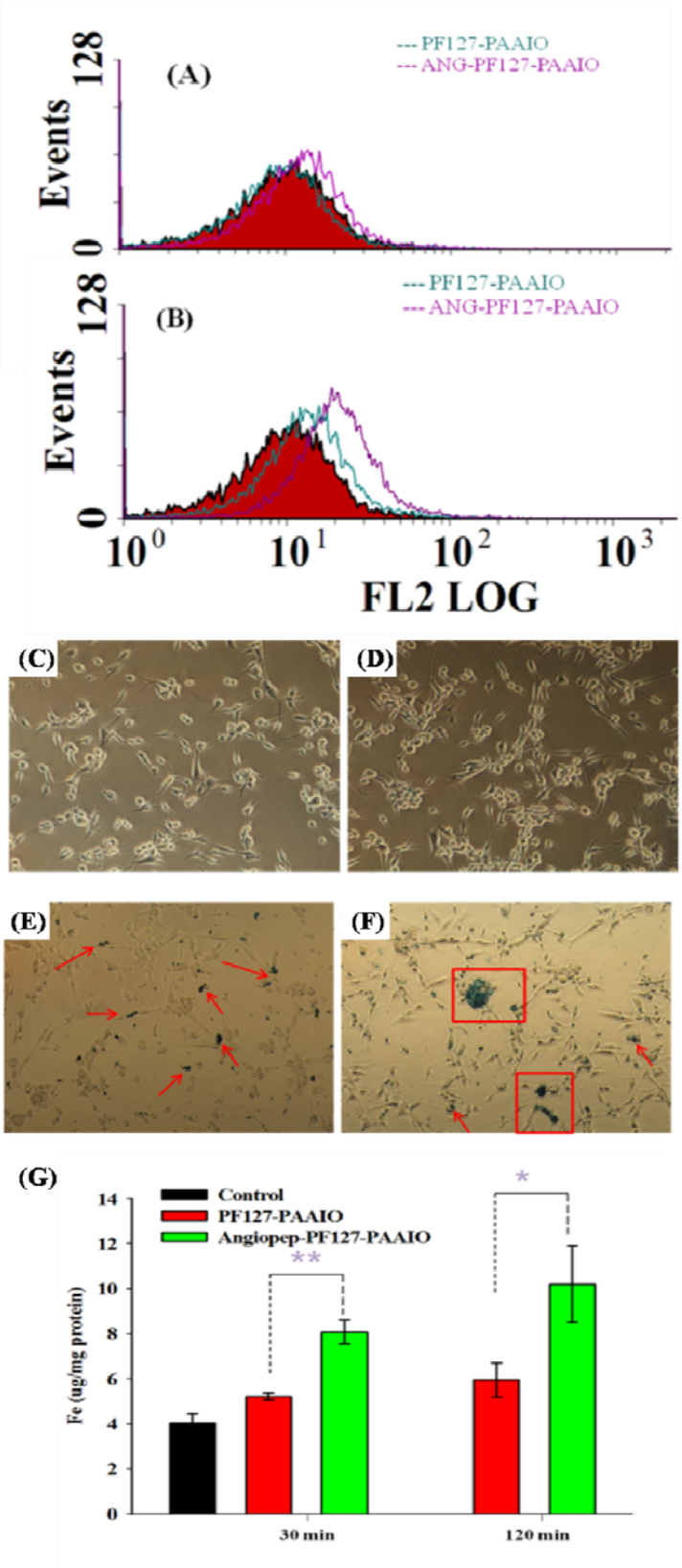
(A)
--- PF127-PAAIO
--- ANG-PF127-PAAIO
Events
128
0
(B)
--- PF127-PAAIO
--- ANG-PF127-PAAIO
Events
128
0
10^0
10^1
10^2
10^3
FL2 LOG
(C)
(D)
(E)
(F)
(G)
Control
PF127-PAAIO
Angiopep-PF127-PAAIO
Fe (ug/mg protein)
14
12
10
8
6
4
2
0
**
*
30 min
120 min

Figure 3.

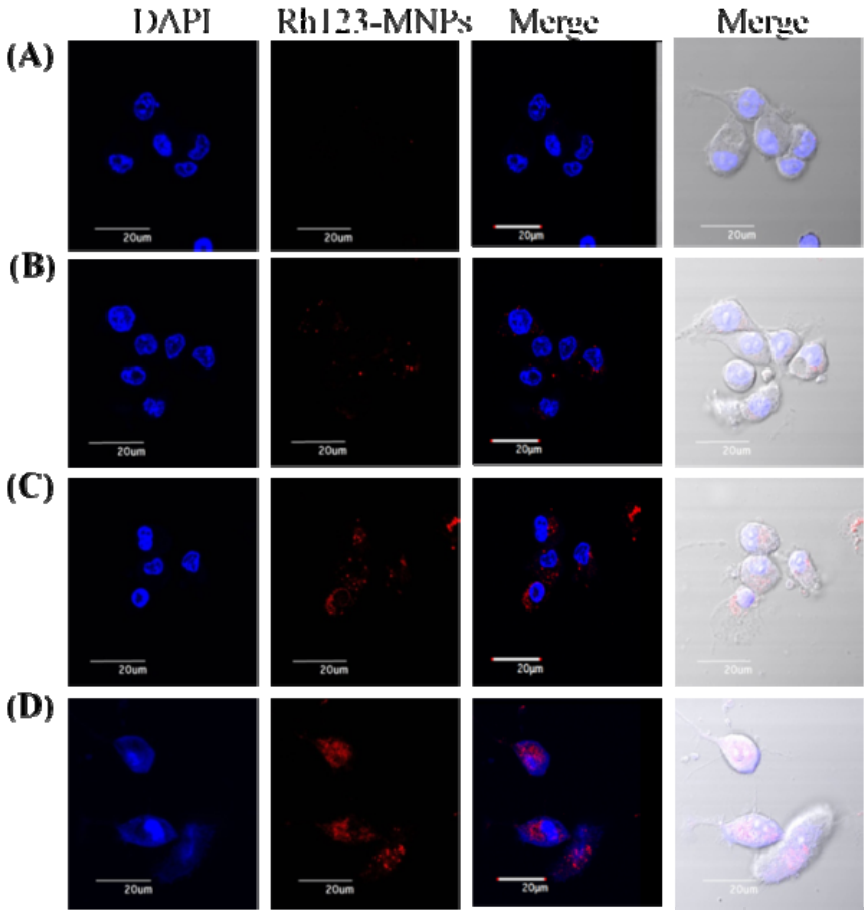

Figure 4.

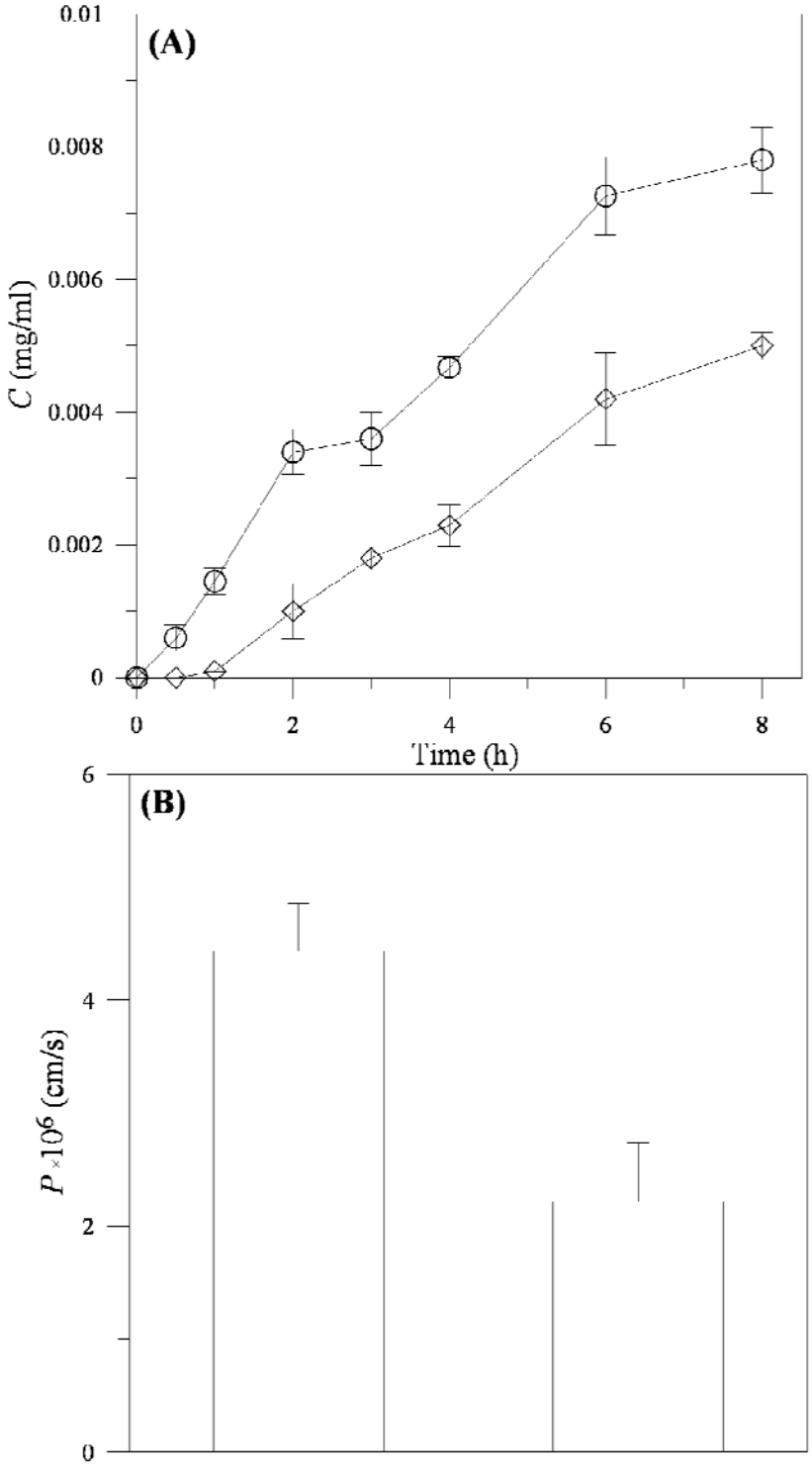

Figure 5.

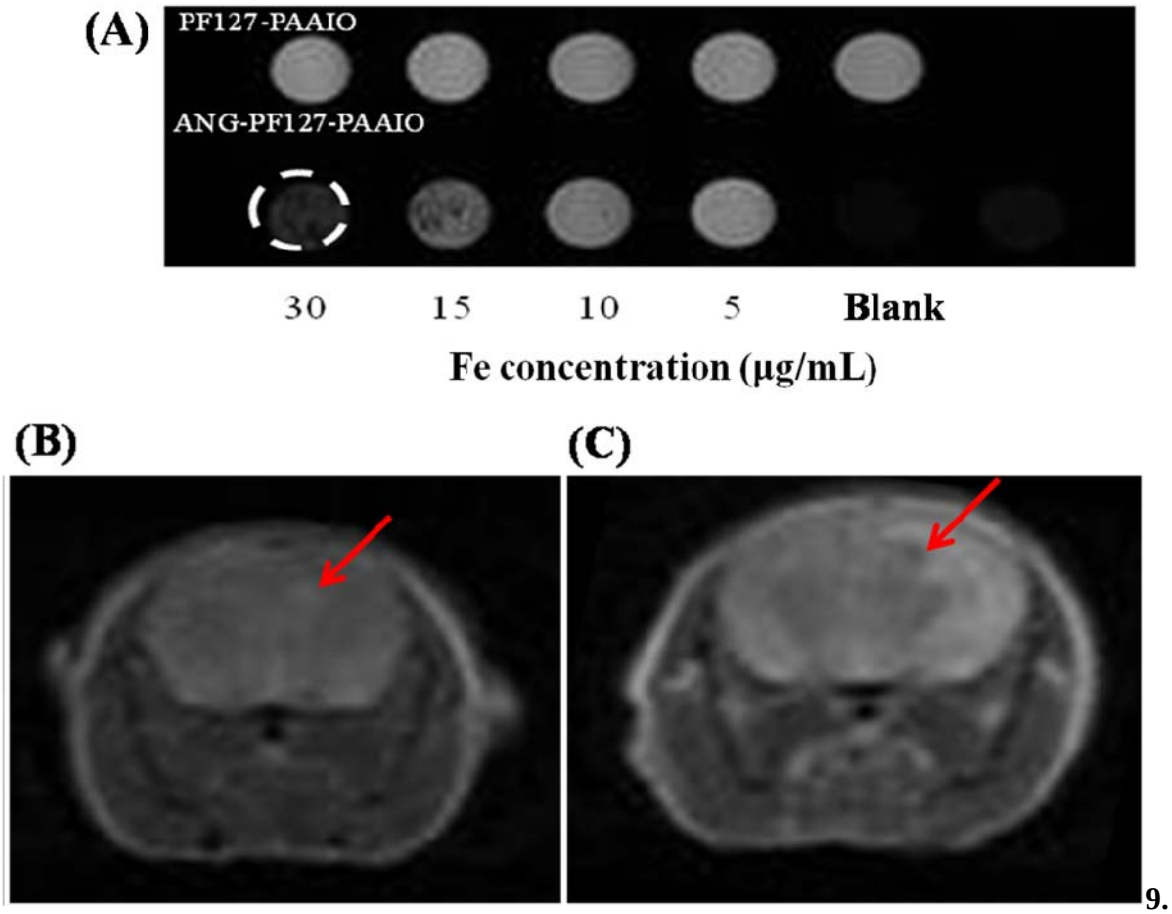
(A)
PF127-PAAIO
ANG-PF127-PAAIO
30
15
10
5
Blank
Fe concentration (μg/mL)
(B)
(C)

9.

Figure 6.

OPEN ACCESS Freely available online

PLOS ONE

Ferrous Citrate Up-Regulates the NOS2 through Nuclear Translocation of NFκB Induced by Free Radicals Generation in Mouse Cerebral Endothelial Cells

Li-Ching Chen[1], Chin Hsu[2], Chuang Chin Chiueh[3], Wen-Sen Lee[1,4,5]*

1 Graduate Institute of Medical Sciences, School of Medicine, Taipei Medical University, Taipei, Taiwan, **2** Department of Physiology, Kaohsiung Medical University, Kaohsiung, Taiwan, **3** Taipei Medical University-Shuang Ho Hospital, Taipei, Taiwan, **4** Department of Physiology, School of Medicine, Taipei Medical University, Taipei, Taiwan, **5** Cancer Research Center, Taipei Medical University Hospital, Taipei, Taiwan

Abstract

Previous studies indicate that the inducible nitric oxide synthase 2 (NOS2) of the brain vascular tissue in experimental subarachnoid hemorrhage (SAH) rats is a critical factor for inducing cerebral vasospasm. However, the underlying molecular mechanisms remain to be elucidated. Here, we applied ferrous citrate (FC) complexes to the primary cultured mouse cerebral endothelial cell (CEC) to mimic the SAH conditions and to address the issue how SAH-induced NOS2 up-regulation. Using immunocytochemical staining technique, we demonstrated that NOS2 was expressed in the cultured CEC. Treatment of the CEC with FC induced increases of the intracellular level of ROS, nuclear factor kappa-light-chain-enhancer of activated B cells (NFκB) nuclear translocation as well as NFκB binding onto the NOS promoter, and the levels of NOS2 mRNA and protein. These effects were abolished by pre-treatment of the cell with N-Acetyl-Cysteine (NAC), a reactive oxygen species (ROS) scavenger. In the present study, two previously predicted NFκB binding sites were confirmed in the NOS2 promoter within the range of −1529 bp to −1516 bp and −1224 bp to −1210 bp. Interestingly, both NFκB binding sites are involved in the FC-activated NOS2 transcriptional activity; the binding site located at −1529 bp to −1516 bp played a greater role than the other binding site located at −1224 bp to −1210 bp in the mouse CEC. These findings highlight the molecular mechanism underlying FC-induced up-regulation of NOS2 in the mouse CEC.

Citation: Chen L-C, Hsu C, Chiueh CC, Lee W-S (2012) Ferrous Citrate Up-Regulates the NOS2 through Nuclear Translocation of NFκB Induced by Free Radicals Generation in Mouse Cerebral Endothelial Cells. PLoS ONE 7(9): e46239. doi:10.1371/journal.pone.0046239

Editor: Alice Y. W. Chang, Kaohsiung Chang Gung Memorial Hospital, Taiwan

Received June 25, 2012; **Accepted** August 29, 2012; **Published** September 28, 2012

Funding: This work was supported by research grants from the National Science Council of Taiwan (NSC-101-2320-B-038-005 and NSC-101-2629-B-037-001 to W.S.L.; NSC-95-2320-B-037-032-MY2 and NSC97-2314-B-037-039-MY2 to C.H.; NSC-95-2320-B-038-027-MY2 to C.C.C.). The funders had no role in study design, data collection and analysis, decision to publish, or preparation of the manuscript.

Competing Interests: The authors have declared that no competing interests exist.

* E-mail: wslee@tmu.edu.tw

Introduction

Hemorrhage stroke, which includes intracerebral hemorrhage and SAH, is associated with high risk of mortality and morbidity. Although the hemorrhage stroke is treated, patients still face the threat of cerebral complications such as rebleeding, recurrent stroke, liquefaction, vasospasm, and hydrocephalus [1].

The pathogenesis of cerebral complications after hemorrhage stroke is complicated and still not fully understood. However, accumulating evidence has suggested that impaired iron metabolism is an initial cause of neurodegeneration, and several common neurodegenerative disorders have been proposed to be associated with dysregulation in CNS iron homeostasis [2–4] and small molecular weight iron complexes [5]. Iron functions as an important cofactor in cellular energy production and contributes to the activity of many proteins and mitochondrial enzymes in most living tissues [6]. Normally, iron is bound and inactivated by transport proteins (e.g. transferrin) and intracellular storage proteins (e.g. ferritin). However, the unbound iron can be found in the brain under some pathological circumstances such as intracerebral hemorrhage. The heme from red blood cells is cleaved into biliverdin by heme oxygenase in astrocytes and microglia, thereby releasing iron [7,8]. The iron released from heme is highly toxic to neurons. Moreover, most of the non-heme iron in the brain is bound to ferritin as ferric ion, and can be released only after being reduced to the ferrous state. Reduction and release of iron from ferritin can be accomplished by superoxide, acidic pH, ascorbate and catecholamines [9,10], which are rich in the extracellular fluid of the brain, especially during hypoxia/ischemia conditions. It has been shown that hypoxia/ischemia conditions cause neuronal cell death and the affected area is accompanied by increased brain levels of iron and ferritin in the cerebral cortex and the hippocampus [11–13]. It has been hypothesized that iron in the ferrous state causes vasospasm. As iron is unbound in the presence of oxygen, it catalyzes the generation of toxic hydroxyl radicals, which could contribute to SAH pathology [7]. The notion that iron plays an important role in the development of SAH was supported by intracerebroventricular injection with ferrous ammonium citrate causing increases of the level of toxic lipid peroxidation products, such as 4-hydroxynonenal (HNE), in the field CA3 of the hippocampus in a rat model [14], and intravenous administration with 2,2′-dipyridyl, an iron chelator, prevents delayed vasospasm in a primate model of SAH [15]. Furthermore, desferal chelates iron complex and prevents the iron-catalyzed oxidative stress and brain injury *in vivo* [16].

Nitric oxide synthase (NOS) consist of different subtypes depending on the tissue type including neuronal (NOS1), inducible or macrophage (NOS2), and endothelial (NOS3) enzyme [17]. NOS1, previously known as non-inducible nNOS, can be induced by ROS generated by serum deprivation or preconditioning stress leading to induction of the redox protein thioredoxin, manganese superoxide dismutase (MnSOD), or Bcl-2 for cytoprotection and survival. NOS2 is inducible and previously named as iNOS. Moreover, NOS3 can also be induced in endothelial cells and lead to vasodilation exerting a protective effect in the early stages of ischemia. ROS can regulate all three subtypes of NOS expression [3,18–20].

Previous *in vivo* studies inferred that an increase of NOS2 expression might play a critical role in the occurrence and progression of the SAH-induced vasospasm [21,22]. However, the molecular mechanisms underlying SAH-induced NOS2 up-regulation is still unclear. In the present study, we applied FC complexes to the mouse primary cultured CEC to mimic the SAH conditions and to address the issue how SAH-induced NOS2 up-regulation.

Materials and Methods

Chemicals

N-acetylcysteine (NAC) was purchased from Sigma-Aldrich (St. Louis, MO, USA). Bay 11-7082, a selective IkappaB kinase (IKK) inhibitor was obtained from Cayman Chemical (Ann Arbor, MI). PDTC, an NFκB inhibitor, was purchased from Sigma-Aldrich. Chemicals used in this study were dissolved in dimethyl sulfoxide (DMSO) or water according to the manufacturer's protocol.

Cell Culture

The CEC was prepared as previously described [23] and all procedures were performed according to the Taipei medical university animal care and use rules (licenses No. LAC-97-0160) and an Association for Assessment and Accreditation of Laboratory Animal Care approved protocol. The surgery was performed under isoflurane anesthesia to minimize suffering. Briefly, the Balb/c mouse was sacrificed by decapitation, meninges and white matter were removed, and cortices were minced and gently dissociated in Hank's balanced salt solution (GIBCO, Grand Island, NY). The resulting microvessel fraction was then sequentially digested with collagenase/dispase at a concentration of 1 mg/mL (Sigma-Aldrich, St. Louis, MO) for 6 h at room

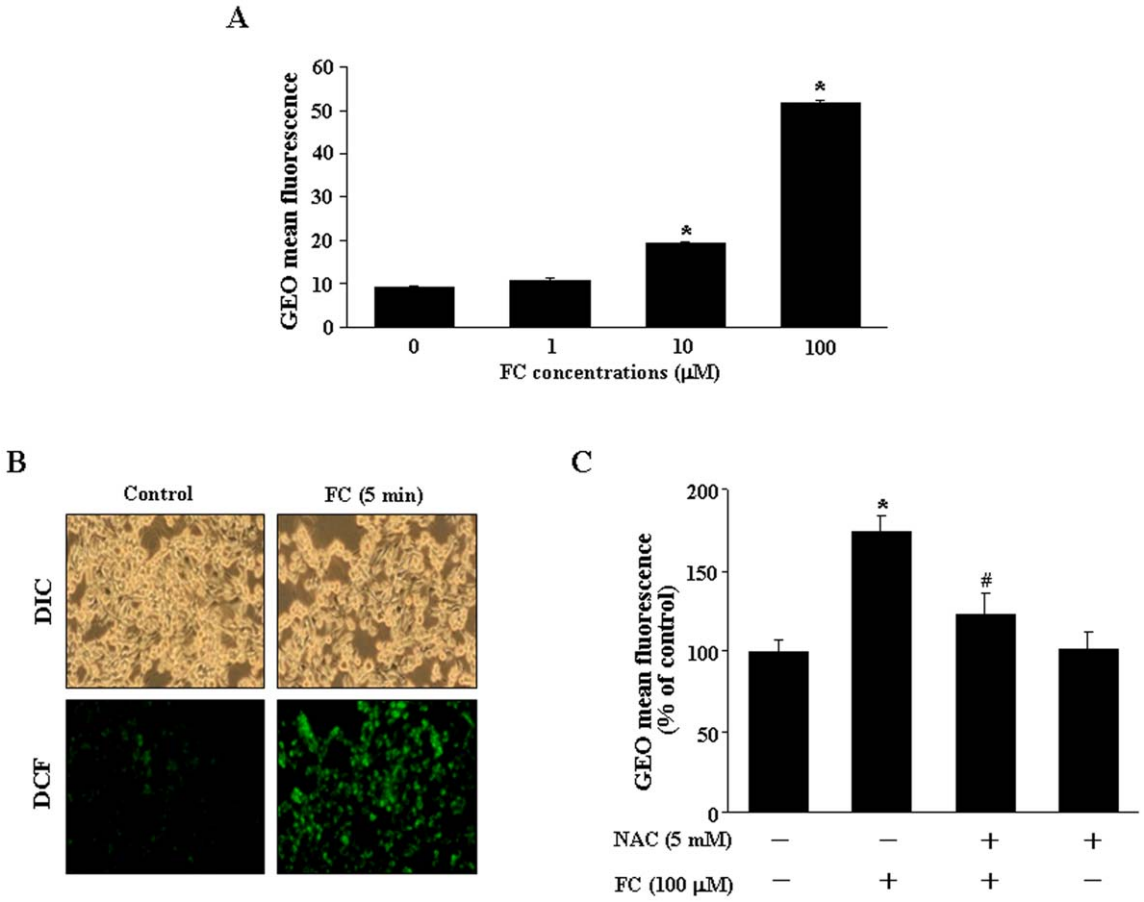

Figure 1. FC increases ROS generation in the CEC. (A) FC (1–100 μM) concentration-dependently increased ROS generation in the CEC. (B) The ROS generation was observed at 5 min after FC (100 μM) treatment. (C) FC (100 μM)-induced increases of ROS generation in CEC were prevented by pretreatment of the cell with a ROS scavenger, NAC (5 mM). ROS levels were assayed using 5 μM DCF as described in Materials and Methods. DCF fluorescence images and DIC images were taken using Leica TCS SP5 fluorescent microscope imaging system (Wetzlar, Germany) and the levels of ROS were quantified by flow cytometric analysis. Values represent the means±s.e.mean. (n = 4). $^{*}P < 0.05$ different from control. $^{\#}P < 0.05$ different from FC-treated group. DIC, differential interference contrast; DCF, dichlorodihydrofluorescein diacetate [CM-H2DCF-DA].
doi:10.1371/journal.pone.0046239.g001

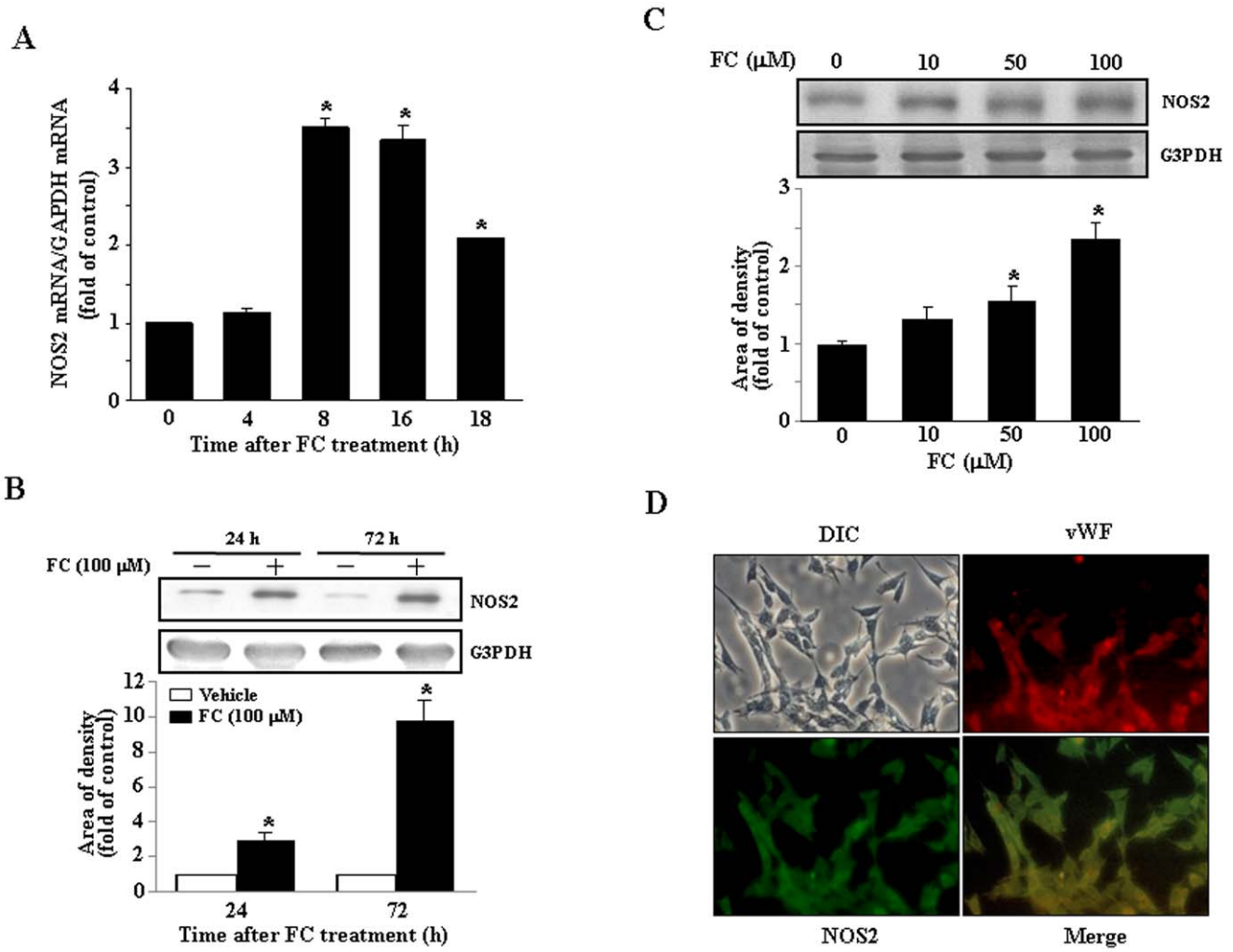

Figure 2. Effects of FC on NOS2 expression in the CEC. (A) The levels of NOS2 mRNA in the CEC were significantly increased at 8 h after FC treatment. A peak of NOS2 mRNA level was observed at 8–16 h after FC treatment, and then began to decline. The levels of NOS2 mRNA were determined using quantitative real time-PCR, adjusted with G3PDH mRNA, and expressed as ratio over control. (B) FC (100 μM) treatment increased the levels of NOS2 protein in the CEC. FC (100 μM) time-dependently increased the level of NOS2 protein. Top panel: representative results of NOS2 and G3PDH protein levels determined by Western blot analysis. Bottom panel: quantitative results of NOS2 protein levels, which were adjusted with G3PDH protein level and expressed as fold-induction of its own control. Values represent the means±s.e.mean. (n = 3). $^{*}P < 0.05$ different from corresponding control. (C) The FC-induced increases of the level of NOS2 protein were in a concentration-dependent manner. Top panel: representative results of the levels of NOS2 and G3PDH protein determined by Western blot analysis. Bottom panel: quantitative results of NOS2 protein levels, which were adjusted with G3PDH protein level and expressed as fold of control. Values represent the means±s.e.mean. (n = 3). $^{*}P <$ 0.05 different from corresponding control. (D) FC-induced NOS2 expression is mainly located in the CEC. Micrographs show NOS2 (green) and vWF (red) immunoreactivity detected by dual immunofluorescent staining as described in Materials and Methods. NOS2, inducible nitric oxide synthase 2; G3PDH, glyceraldehyde3-phosphate dehydrogenase, vWF, von Willebrand Factor.
doi:10.1371/journal.pone.0046239.g002

temperature. After centrifugation, the pellet containing the CEC was washed with Dulbecco's modification of Eagle's medium (DMEM, GIBCO), maintained in DMEM supplemented with 10 % fetal bovine serum (FBS) in a humidified incubator (37°C, 5% CO_2). CEC showed positive immunoreactivity for Von Willebrand factor (vWF), a marker for endothelial cells. Cells from passages 10 to 25 were used.

FC Treatment

The FC complex was prepared as previously described [14,24]. Ferrous ammonium sulfate and citric acid (Sigma-Aldrich) were dissolved in sterile distilled water and the pH was adjusted to 7.4 with NaOH. A concentration of 100 μM FC was freshly prepared prior to each treatment by mixing 1:1 volume of 200 μM ferrous ammonium sulfate and 200 μM citric acid.

Measurement of ROS

For measurement of intracellular ROS levels, cells were incubated with 5 μM 5- (and-6)-chloromethyl-2,7-dichlorodihydrofluorescein diacetate acetyl ester [CM-H2DCFDA (here referred to as DCF) (Invitrogen, Carlsbad, CA)] for 10 min, and then washed with phosphate-buffered saline (PBS). The fluorescence and differential interference contrast images were taken using Leica TCS SP5 fluorescent microscope imaging system (Wetzlar, Germany) and analyzed by flow cytometry according to the manufacturer's instructions (Becton Dickinson, San Jose, CA).

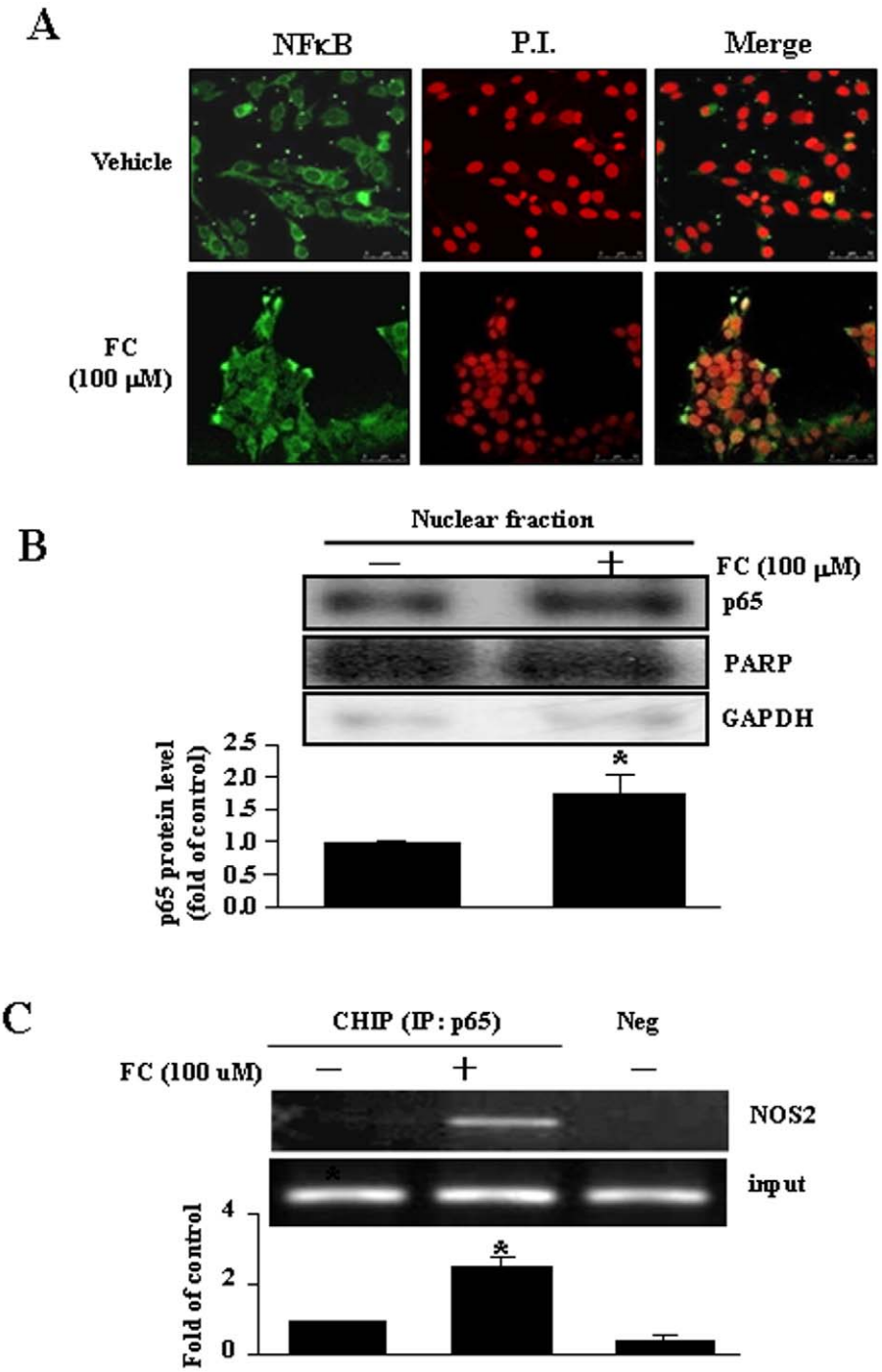

Figure 3. Involvement of NFκB (p65) in regulating the NOS2 promoter activity in the FC-treated CEC. (A) FC (100 μM) induced NFκB translocation from the cytosolic fraction into the nuclear fraction in the CEC. After treatment with FC for 4 h, the CEC was fixed and then labeled with an anti-NFκB antibody, followed by an FITC-conjugated secondary antibody. The nuclei were visualized with propidium iodide (50 μg/mL) staining as described in Materials and Methods. (B) FC (100 μM) increased nuclear translocation of NFκB in the CEC. Top panel: representative results of NFκB, PARP and G3PDH protein levels determined by Western blot analysis. Bottom panel: quantitative results of NFκB protein levels, which were adjusted with PARP protein level and expressed as fold of control. Values represent the means±s.e.mean. (n = 4). $^{*}P < 0.05$ different from corresponding control. (C) FC (100 μM) induced an increase of NFκB binding onto the NOS2 promoter. The levels of NFκB binding onto the NOS2 promoter were assessed by using ChIP assay (top panel) and quantitative real-time PCR (bottom panel). Values represent the means±s.e.mean. (n = 4). $^{*}P < 0.05$ different from control. P.I., propidium iodide.
doi:10.1371/journal.pone.0046239.g003

RNA Isolation and Real-time Quantitative PCR

Total RNA was isolated from the CEC using Trizol (Invitrogen) according to the manufacturer's protocol. The NOS2 subunit-specific primers were synthesized as described previously [25]. A LightCycler thermocycler (Roche Molecular Biochemicals, Mannheim, Germany) was used for the real-time PCR. The NOS2

A

Sense and antisense primers used in cloning mouse NOS2 promoter and in generating different constructs

Constructs (kb)	Sense (5'→3')
NOS2 (1.6)	CCACAGAGTGATGTAATCAAG
NOS2 (1.25)	GGAAGACACTCCTAAGAGCAG
NOS2 (0.9)	AGCAATGAGTTTCAGTTAACT
NOS2 (0.48)	ACTAATGACAAGTGCTTGCCC
NOS2 (0.25)	TCTTTGTAGAACTGGAGTCTG
Antisense	GTCTGAGACTTTGCACTTCTG
Constructs (bp)	Sense (5'→3') and Anti Sense (5'→3')
-1201→-1280 (fragment A)	ACTGCAAGGTGAGTCTTGTGT AAGCCTGGTTTTCTGGGCTTT
-1231→-1600 (fragment B)	CCACAGAGTGATGTAATCAAG CTGCTCTTAGGAGTGTCTTCC
-1211→-1600 (fragment C)	CCACAGAGTGATGTAATCAAG TTTCTGGGCTTTCCCAAGCAG

B

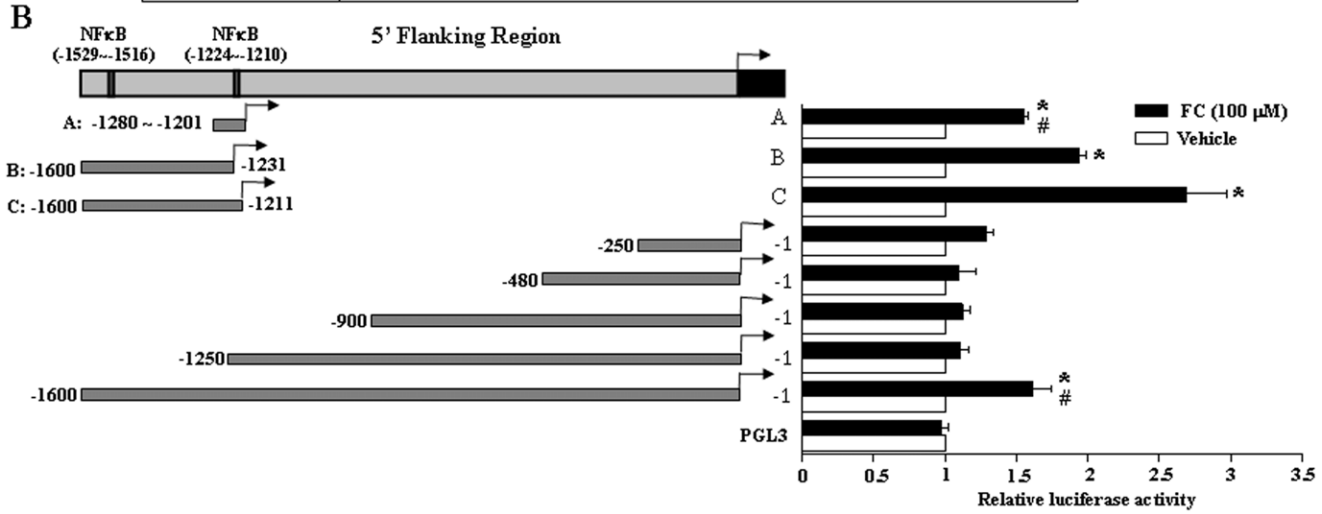

Figure 4. NFκB-binding sites are required for the FC-induced NOS2 promoter transactivation. 5′-serial deletions of the mouse NOS2 1.6-kb promoter were generated by PCR as described in "Materials and Methods" by using the primers indicated in (A). (B) The CEC was transiently transfected with various constructs for 24 h, and then treated with vehicle or FC (100 μM) for 16 h. Subsequently, the cell was processed for the luciferase activity assay. Quantitative results of the NOS2 promoter activity were shown and expressed as fold induction of the CEC transfected with PGL3 (control). Values represent the means±s.e.mean. (n = 4). $^{*}P < 0.05$, different from cells transfected with PGL3; $^{\#}P < 0.05$, different from cells transfected with −1211 to −1600. C, Control.
doi:10.1371/journal.pone.0046239.g004

mRNA fluorescence intensity was measured and normalized with the level of glyceraldehydes-3-phosphate dehydrogenase (G3PDH) using the built-in Roche LightCycler Software Version 4.

Reverse Transcriptase-polymerase Chain Reaction (RT-PCR) Analysis

The RT-PCR assays for NOS2 gene expression were performed as described previously [26]. The cell was treated with the FC complex for 18 h, and then processed for total RNAs isolation using Trizol reagent according to manufacturer's protocol (Invitrogen). The cDNA was amplified from 1 μg of total RNA using a SuperScript one-step RT-PCR with platinum Taq system (Life Technologies, Karlsruhe, Germany). PCR was conducted for 35 cycles in thermal controller. Primers used for amplification were as follows: NOS2 5′-TGCTGTTCTCAGCCCAACAA-3′, and reverse: 5′-GAACTCAATGGCAT GAGGCA-3′. The polymerase chain reaction primers for G3PDH were forward primer: 5′-GCATGGCCTTCCGTGTTCCTA-3′, and reverse primer: 5′-CCTTCAGTGGGCCCTCAGATG-3′. The amplification profile involved denaturation at 94°C for 1 min, primer annealing at 58°C for 30 sec, extension at 72°C for 1 min, and repeated for 35 cycles.

Western Blot Analysis

Western blot analysis was performed as described previously [27]. Briefly, cell lysates were prepared, electrotransferred, immunoblotted with antibodies, and then visualized by incubating with the enhanced chemiluminescence system (Amersham, Buckinghamshire, England). Monoclonal mouse NFκB and total nuclear factor of kappa light polypeptide gene enhancer in B-cells inhibitor, alpha (IκBα) antibodies, as well as polyclonal rabbit Poly ADP-ribose polymerase (PARP) and vWF antibodies were purchased from Santa Cruz, (CA, USA). Monoclonal mouse NOS2 and phospho-IκBα (p-IκBα) antibodies were purchased from BD Bioscience (Clontech) and Cell Signaling Technology (Beverly, USA), respectively. The level of G3PDH (Abcam, Cambridge, MA) was detected and used as the control for equal protein loading. The intensity of each band was quantified by densitometry analysis using Image Pro Plus 4.5 software program

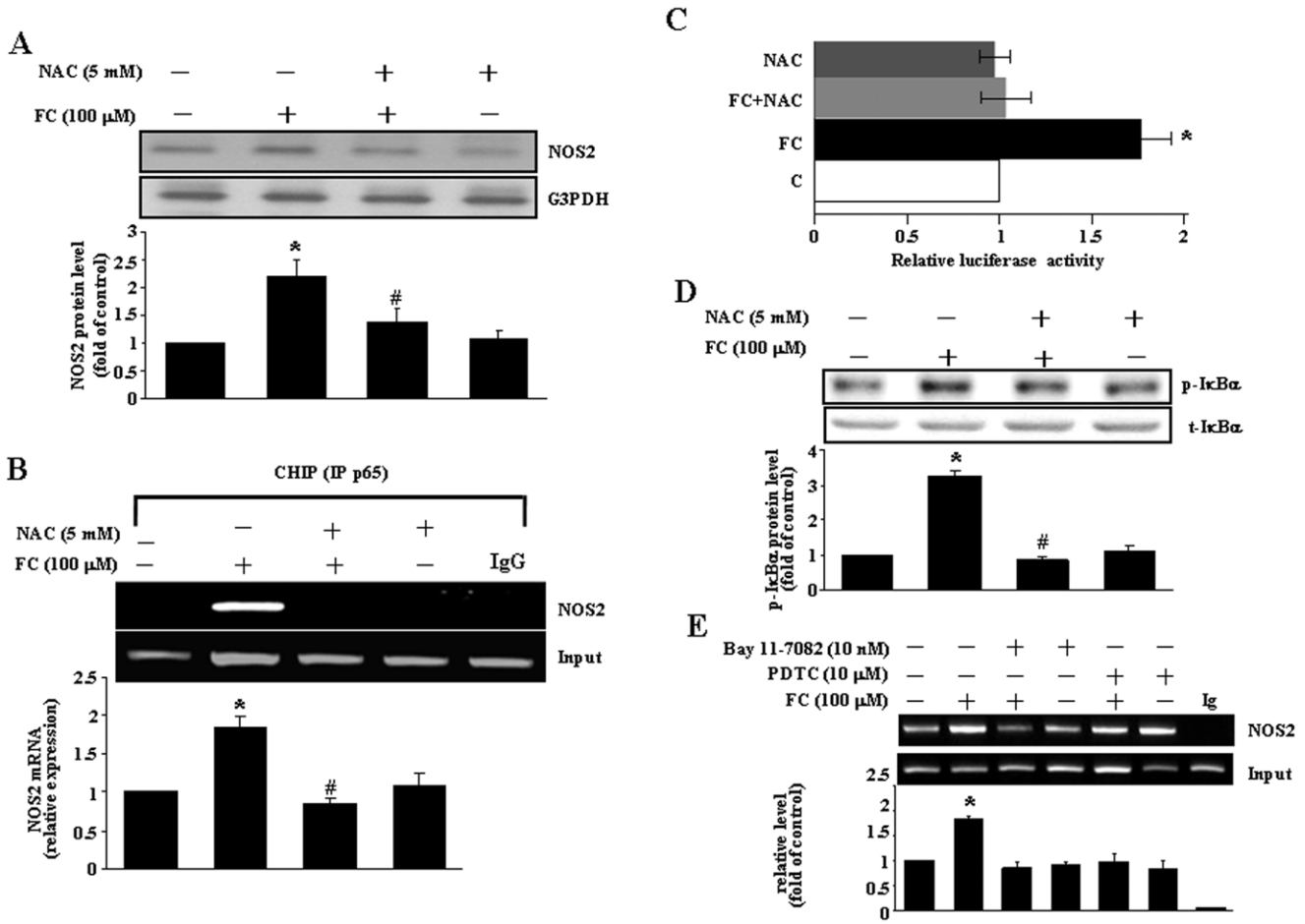

Figure 5. FC induces NFκB activation through increases of the levels of ROS and phosphorylated IκBα. (A) Pretreatment of the CEC with a ROS scavenger, NAC (5 mM), for 1 h prevented the FC-induced increases of the levels of NOS2 protein. Top panel: representative results of NOS2 and G3PDH protein levels determined by Western blot analysis. Bottom panel: quantitative results of NOS2 protein levels, which were adjusted with G3PDH protein level and expressed as fold of control. Values represent the means±s.e.mean. (n = 3). $^{*}P < 0.05$ different from corresponding control; $^{\#}P < 0.05$ different from the FC-treated CEC. (B) The FC (100 μM)-induced an increase of the NFκB (p65) DNA binding onto the NOS2 promoter was completely abolished by pretreatment of the cell with NAC (5 mM). The NOS2 DNA binding activity was assessed by using ChIP assay and detected by semiquantitative PCR (top panel) and quantitative real-time PCR (bottom panel). Values represent the means±s.e.mean. (n = 3). $^{*}P < 0.05$ different from corresponding control; $^{\#}P < 0.05$ different from the FC-treated CEC. (C) FC-induced an increase of the NOS2 promoter activity was abolished by pretreatment of the cell with NAC. Values represent the means±s.e.mean. (n = 3). $^{*}P < 0.05$, different from control. (D) Pretreatment of the CEC with NAC (5 mM) for 1 h prevented the FC-induced increases of the levels of phosphorylated IκBα (p-IκBα) protein. Top panel: representative results of the levels of p-IκBα and total IκBα (t-IκBα) protein determined by Western blot analysis. Bottom panel: quantitative results of p-IκBα protein levels, which were adjusted with t-IκBα protein level and expressed as fold of control. Values represent the means±s.e.mean. (n = 3). $^{*}P < 0.05$ different from corresponding control; $^{\#}P < 0.05$ different from the FC-treated CEC. (E) FC increased phosphorylation of the protein IκBα and NFκB binding on the NOS2 promoter, and these effects were blocked by a ROS scavenger (NAC), an IKK inhibitor (Bay 11-7082), or NFκB translocation inhibitors (PTDC). The levels of NOS2 protein were quantified by Western blot analysis. The NFκB DNA binding activity was assessed by using ChIP assay and quantitative real-time PCR (bottom panel). Values represent the means±s.e.mean. (n = 3). $^{*}P < 0.05$, different from corresponding control; $^{\#}P < 0.05$, different from FC-treated without ROS scavenger (NAC).
doi:10.1371/journal.pone.0046239.g005

(Media Cybernetics, Silver Spring, MD) and pixel densities were normalized to that of the loading control in Western blot analysis.

Immunocytochemical Staining

The CEC was seeded on glass coverslips, treated with vehicle or FC (100 μM) for 4 h, washed three times with PBS, and then fixed with 4% formaldehyde in PBS for 15 min. Cells were placed in blocking solution (PBS containing 15% FBS, 2% bovine serum albumin (BSA), and 0.1% saponin) for 45 min at room temperature, and then incubated with anti-NFκB Fluorescein isothiocyanate (FITC)-conjugated monoclonal antibody at a 1:100 dilution for 1 h at room temperature in blocking solution. To visualize nuclei, DNA was stained with propidium iodide (50 μg/mL in PBS and 0.1% BSA) for 5 min. After washing three times with PBS, cells were viewed under a laser confocal spectral microscope imaging system (Leica, TCS SP5, Bannockburn, IL, USA).

Chromatin Immunoprecipitation Analysis (ChIP)

ChIP assays were performed as described previously [28]. The anti-NFκB antibody (Santra Cruz) was used for immunoprecipitation reactions. Primers specific for the detection of transcription factor binding regions from −460 bp to −250 bp of the NOS2 gene were designed. The sense primer was 5′–GGATACACCA-

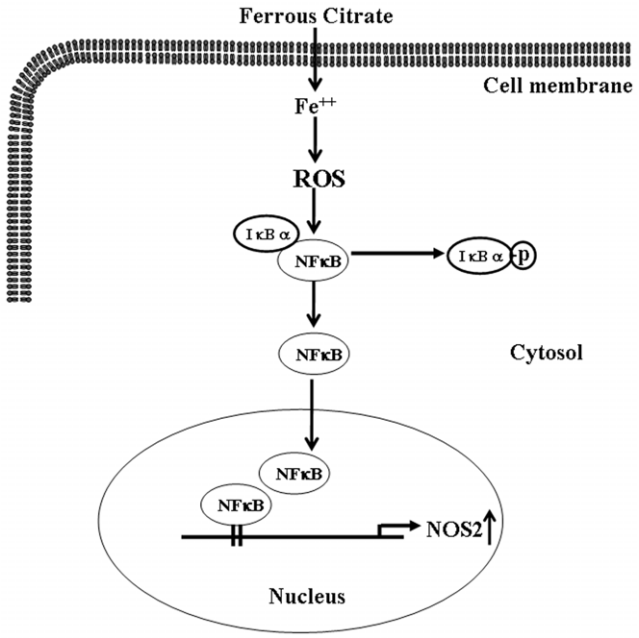

Figure 6. Proposed signaling pathway associated with FC-induced up-regulation of NOS2 in the CEC. FC increased ROS generation, which in turn caused IκBα phosphorylation, subsequently increased NFκB (p65) nuclear translocation and binding onto the NOS2 promoter, and finally increased the levels of NOS2 mRNA and protein.
doi:10.1371/journal.pone.0046239.g006

CAGAGTGATG-3′, and the anti-sense primer was 5′-CATAT-CAGCTTCAGTCCAGC-3′.

Construction of the *NOS2* Gene Promoter Plasmid

The 1600-bp fragment of the mouse *NOS2* promoter was amplified by genomic PCR using genomic DNA from the CEC as the template. The primers of 5′-CCACAGAGTGATGTAAT-CAAG-3′ and 5′ GTCTGAGACTTTGCACTTCTG-3′ were used. This PCR fragment was ligated into a basic luciferase reporter gene in the pGL3 vector (Promega, Madison, WI, USA) with Mlu1 and XhoI restriction sites, and designated as PGL3 NOS2. The pRL-TK vector encodes the Renilla luciferase gene, which was used as an internal control to normalize for pGL3 firefly luciferase expression. The sequence was confirmed by ABI 3730XL analysis system (Applied Biosystems Inc., Foster City, CA).

Cell Transfection and Dual Luciferase Reporter Assay

For transient transfection, Lipofectamine^{TM} 2000 transfection reagent (Invitrogen) was used according to the manufacturer's protocol. Briefly, Lipofectamine and plasmid DNA (PGL3 NOS2 3.5 μg and 50 ng of pRL-TK) was added to each well containing cells and Opti-MEMR I Medium, and then incubated in a humidified incubator at 37°C for 4 h. The medium was replaced and the cell was then incubated for an additional 24 h. After incubation, the cell was treated with FC (100 μM) for 16 h, lysed in passive lysis buffer (Promega), and then mixed with luciferase assay substrate (Dual-Glo luciferase reporter system; Promega). The Firefly and Renilla luciferase activities were measured with a 96-well luminometer and analyzed by skanIt^{TM} software2.4.1. (Thermo Fisher Scientific, Rocford, IL).

Statistics

All data were expressed as the mean value ± s.e.mean. Comparisons were subjected to one way analysis of variance (ANOVA) followed by Fisher's least significant difference test. Significance was accepted at $P < 0.05$.

Results

FC Increases ROS Levels in the CEC

It has been indicated that iron can potentiate ROS production and exacerbate oxidative stress [29,30]. To study the effect of iron on the production of ROS, the mouse CEC was treated with various concentrations of FC, small molecular weight iron complex, and the levels of ROS were measured by DCF. FC (1–100 μM) concentration-dependently increased the ROS level in the CEC (Fig. 1A). The FC-induced an increase of the ROS level was observed as early as 5 min after treatment (Fig. 1B). Pretreatment of the CEC with a ROS scavenger, NAC (5 mM), prevented the FC-induced increases of ROS (Fig. 1C).

FC Increases the Levels of NOS2 mRNA and Protein in the CEC

Previously, we demonstrated that SAH caused an increase of NOS2 production in the rat basilar artery [21]. In addition, ROS has been suggested to play an important role in regulating multiple proinflammatory genes, such as *NOS1* [31] and *NOS2* [3]. Accordingly, we examined whether FC complex could induce NOS2 expression in the subcultured CEC. The level of NOS2 mRNA was significantly increased in the CEC at 8 h after FC treatment, and then began to decline at 18 h (Fig. 2A). FC (100 μM) treatment also time-dependently increased the level of NOS2 protein in the CEC (Fig. 2B). The FC-induced increases of the level of the NOS2 protein were in a concentration-dependent manner (Fig. 2C). To confirm that the expression of NOS2 protein was localized in endothelial cells but not from the culture contaminated with other cell types, immunocytochemical staining was performed. As illustrated in Figure 2D, NOS2 immunoreactivity was co-localized with Von Willebrand Factor, a marker for endothelial cells, suggesting that the NOS2 protein detected in the present study was mainly produced by the CEC. The expression of NOS3 mRNA and protein was not significantly altered (unpublished observation).

FC Increases NFκB Nuclear Translocation and NFκB Binding onto the NOS2 Promoter

NFκB is a key transcription factor involved in the regulation of NOS2 expression [32]. The present study examined whether FC small molecular iron complexes could induce nuclear translocation of NFκB. In the control culture, NFκB was mainly located in the cytoplasm of the CEC. Following FC (100 μM) treatment, NFκB was translocated from the cytoplasm into the nucleus as evidenced by colocalization of the NFκB immunoreactivity and propidium iodide (PI) staining (Figs. 3A and 3B). FC-induced nuclear translocation of NFκB (p65) began at 30 min after treatment and lasted for 8 h (data not shown). ChIP assays revealed that the nuclear NFκB was bound to the NOS2 promoter in the CEC (Fig. 3C), suggesting that there was a transcription activation effect of FC complex on the mechanisms for NOS2 gene expression in the subcultured CEC.

Effect of FC on NFκB-binding Sites in the Promoter Region of the NOS2 Gene

To map the regulatory regions of the mouse NOS2 promoter, the present study employed the serial deletion strategy by constructing recombinant plasmids containing different 5′-deletions of the mouse NOS2 promoter linked to a luciferase reporter gene. The full length of the mouse NOS2 5′ flanking region (1.6 kb) was cloned by PCR using mouse genomic DNA as a template (Fig. 4A). Serial deletions of the mouse NOS2 promoter (0.25 kb, 0.48 kb, 0.9 kb, and 1.25 kb) were generated by using the cloned mouse NOS2 promoter as a template and the primers were shown in Figure 4A. As shown in Figure 4B, the NOS2 promoter luciferase activity was 1.7 fold increased in the CEC transfected with the full length of the promoter (−1 bp to −1600 bp) and activated by FC (100 μM) as compared with those transfected with control vector. Deletions from 5′ end of the promoter to −1250 bp, −900 bp, −480 bp and −250 bp (Fig. 4B) yield no luciferase activity, indicating that the promoter −1211 bp to −1600 bp region might be necessary for the promoter activity through NFκB activation. To determine which NFκB binding sites is crucial for the NOS2 gene activation after treated with FC (100 μM), three more constructs (fragment A: −1201 bp to −1280 bp, fragment B: −1211 bp to −1600 bp, and fragment C: −1231 bp to −1600 bp) of NOS2 based on previously predicted two NFκB binding sites on the NOS2 promoter were prepared. As shown in Figure 4 B, luciferase activities of fragment A with one of the functional NFκB binding site (−1224 bp to −1210 bp) was approximately 95% of the full length activity. Fragment B contained the secondary functional NFκB binding site (−1529 bp to −1516 bp) was 1.2 times greater than the full length activity. Fragment C contained both NFκB binding sites evoked 2.6 times activity. Thus, these data suggest that both regions of the NFκB binding sequences are necessary for the maximal NOS2 promoter activity after treated with FC.

FC Increases NOS2 Expression through ROS Production

The putative effect of ROS on NOS2 expression was studied. To investigate whether antioxidant blocks the FC-induced up-regulation of NOS2, the CEC was pretreated with 5 mM of NAC for 30 min followed by 100 μM FC, and incubated for 24 h. At the end of incubation, cells were harvested for assay. Pretreatment of the cell with NAC prevented the FC-induced increases of transcription of the NOS2 protein (Fig. 5A), NFκB binding onto the NOS2 promoter (Fig. 5B), and the NOS2 promoter activity (Fig. 5C). We also examined whether FC-induced NFκB nuclear translocation in the CEC through ROS-mediated IκBα phosphorylation. As shown in Figure 5D, pretreatment of the CEC with NAC prevented the FC-induced phosphorylation of IκB. In addition, pretreatment of the CEC with Bay 11-7082 (a selective IKK inhibitor) or PDTC (an NFκB inhibitor) abolished the FC-induced increases of the binding of NFκB protein onto the NOS2 promoter (Fig. 5E), suggesting that FC-induced NFκB nuclear translocation was mediated by IκB phospohrylation.

Discussion

Intracerebral injection of lysed blood, hemoglobin, and FC causes neurodegeneration due to redox cycling of iron complex, increases in hydroxyl radical, lipid peroxidation, oxidative stress, and brain injury [33]. Low dosages of FC (less than 20 nmole) produce dopaminergic toxicity in the midbrain substantial nigra that can be prevented by S-Nitrosoglutathione (GSNO) and NO [34]. In clinical observation, vasospasm is often triggered by lysed blood after SAH, a ruptured brain aneurysm, and bleeding in cerebral spinal fluid of ventricular space. Moreover, 2,2′-dipyridyl, a ferrous iron chelator, prevents delayed vasospasm in a primate model of SAH [15]. Consistently, a review article indicated that ferrous ion might be involved in vasospasm development [35].

In the mouse CEC, FC (0.1 mM) generated ROS, produced little cytotoxicity (unpublished observations), but up-regulated the expression of NOS2 (Figs. 2A, B and C). The induction of NOS2 was triggered by ROS because it was blocked by NAC pre-treatment. In previous studies, antioxidants and GSNO/NO prevent the ROS-evoked oxidative stress via the induction of NOS1 expression and related new protein synthesis such as MnSOD, Bcl-2, and thioredoxin [34]. ROS can activate voltage sensitive calcium channel and increase intracellular calcium that could lead to vasospasm [36,37]; all of which can be blocked by nimodipine, a calcium channel blocker.

NOS2 has been implicated as an important mediator of inflammatory responses during ischemia and reperfusion in rodents [38–43]. Rodent NOS2 can be induced by ROS generated by bacterial lipopolysaccharides, interferon-gamma [44,45] or FC (Fig. 5A). However, the functions of up-regulation of NOS2 in the mouse CEC remain to be studied. The regulation of NOS2 expression is quite complex as it involves a variety mechanisms within a wide range of cell types and species difference. It is known that the human NOS2 promoter is different from that in the mouse by more than 50% [46], suggesting that the functions of NOS2 may have species differences. In AKN1 human liver cells, the induction of NOS2 by cytokine stimulation is mediated by NFκB binding onto the NOS2 promoter ranging from −4,700 bp to −16,000 bp [47]. In the mouse CEC, however, NFκB up-regulated the NOS2 promoter at two functional binding sites near −1500 bp and −1200 bp (Fig. 4). Transfection of the CEC with the construct containing both functional NFκB binding sites (−1211 bp to −1600 bp) induced a significantly higher NOS2 activity as compared with the construct containing only one NFκB binding site (−1201 bp to 1280 bp or −1231 bp to −1600 bp) or a full length of the promoter region (−1 bp to −1600 bp), suggesting that the downstream of the first potential NFκB binding site might contain a binding site for negative regulatory protein. This notion was supported by the result that transfection of the CEC with the construct containing the −1 bp to −1250 bp region, which covered one of the potential NFκB binding site (−1210 bp to −1224 bp), did not induce any significant change of the NOS2 promoter activity. Therefore, NFκB activation of the NOS2 promoter in human is different from that of mouse. To clarify this issue of ROS-activated NFκB for the induction of NOS2, additional future studies need to be performed. The present finding of two functional NFκB binding sites for activation of the mouse NOS2 promoter is in agreement with two proposed NFκB binding sites on the mouse NOS2 promoter based on the Transcriptional search database system (http://www.cbrc.jp/research/db/ TFSEARCH. html).

Nuclear translocation of NFκB (Fig. 3) was mediated by phosphorylation of IκBα, which released NFκB from the complex of IκB-NFκB leading to the translocation of NFκB from the cytoplasm pool to the nucleus and binding onto the promoter for NOS2 transcription. Pre-treatment of the CEC with NAC, a ROS scavenger, prevented the FC-induced increases of IκBα phosphorylation (Fig. 5D), NFκB binding onto the NOS2 promoter (Fig. 5E), the NOS2 promoter activity (Fig. 5C), and the level of NOS2 protein (Fig. 4A). Taken together, these data suggest that an increase of ROS might contribute to FC-induced up-regulation of NOS2 through activation and binding of NFκB onto the NOS2 promoter of the mouse CEC. These results are consistent with

early reports [44,48]. However, the issue of how IKK is activated after FC treatment has not been addressed in this study. A previous study on cultured vascular smooth muscle cells has suggested that statins diminish NFκB activation elicited by oxidative stress through the inhibition of IKK-1/-2, p38 mitogen-activated protein kinase (MAPK), and p42/44 MAPK activation [49]. The molecular mechanism underlying ROS-induced IKK activation in the FC-treated CEC is still not clear and deserves further investigation. Since NOS2 could play central roles in inflammation mediated by microglia and macrophages in the central nervous system, it will be interested to know whether the similar pathways are involved in NOS2 induction in other inflammatory cells after ischemia or FC treatment. Although increases of interferon-γ-inducible macrophage nitric oxide generation through the NFκB-dependent pathway [50] and involvement of ROS in activation of NFκB in neutrophils [51] have been demonstrated, the direct evidence for molecular signaling pathways involved in ischemia- or FC-induced NOS2 induction in microglia or macrophages has not been found. Whether this signaling pathway involved in the FC-induced NOS2 induction is unique to cerebral endothelial cells still needs further investigation. In conclusion, this study provides evidence that ROS produced by FC small molecular weight iron complex caused no apparent cytotoxicity in the mouse CEC, while activated phosphorylation of IκB and nuclear translocation of NFκB resulted in activation of the NOS2 promoter and related protein transcription (Fig. 6). The most interesting findings are the identification of two functional NFκB binding sites for the activation of the mouse NOS2 promoter.

Author Contributions

Conceived and designed the experiments: LCC CH CCC WSL. Performed the experiments: LCC. Analyzed the data: LCC CH CCC WSL. Contributed reagents/materials/analysis tools: WSL. Wrote the paper: LCC CCC WSL.

References

1. Dumont AS, Dumont RJ, Chow MM, Lin CL, Calisaneller T, et al. (2003) Cerebral vasospasm after subarachnoid hemorrhage: putative role of inflammation. Neurosurgery 53: 123–133; discussion 133–125.
2. Mills E, Dong XP, Wang F, Xu H (2010) Mechanisms of Brain Iron Transport: Insight into Neurodegeneration and CNS Disorders. Future Med Chem 2: 51–64.
3. Defrere S, Lousse JC, Gonzalez-Ramos R, Colette S, Donnez J, et al.. (2008) Potential involvement of iron in the pathogenesis of peritoneal endometriosis. Mol Hum Reprod 14: 377–385
4. Chen TY, Tsai KL, Lee TY, Chiueh CC, Lee WS, et al. (2010) Sex-specific role of thioredoxin in neuroprotection against iron-induced brain injury conferred by estradiol. Stroke 41: 160–165.
5. Chiueh CC (2001) Iron overload, oxidative stress, and axonal dystrophy in brain disorders. Pediatr Neurol 25: 138–147.
6. Sorond FA, Ratan RR (2000) Ironing-out mechanisms of neuronal injury under hypoxic-ischemic conditions and potential role of iron chelators as neuroprotective agents. Antioxid Redox Signal 2: 421–436.
7. Bishop GM, Robinson SR (2001) Quantitative analysis of cell death and ferritin expression in response to cortical iron: implications for hypoxia-ischemia and stroke. Brain Res 907: 175–187.
8. Hua Y, Keep RF, Hoff JT, Xi G (2007) Brain injury after intracerebral hemorrhage: the role of thrombin and iron. Stroke 38: 759–762.
9. Allen DR, Wallis GL, McCay PB (1994) Catechol adrenergic agents enhance hydroxyl radical generation in xanthine oxidase systems containing ferritin: implications for ischemia/reperfusion. Arch Biochem Biophys 315: 235–243.
10. Biemond P, Swaak AJ, van Eijk HG, Koster JF (1988) Superoxide dependent iron release from ferritin in inflammatory diseases. Free Radic Biol Med 4: 185–198.
11. Ishimaru H, Ishikawa K, Ohe Y, Takahashi A, Tatemoto K, et al. (1996) Activation of iron handling system within the gerbil hippocampus after cerebral ischemia. Brain Res 726: 23–30.
12. Kondo Y, Ogawa N, Asanuma M, Ota Z, Mori A (1995) Regional differences in late-onset iron deposition, ferritin, transferrin, astrocyte proliferation, and microglial activation after transient forebrain ischemia in rat brain. *J Cereb Blood* Flow Metab 15: 216–226.
13. Palmer C, Menzies SL, Roberts RL, Pavlick G., Connor JR (1999) Changes in iron histochemistry after hypoxic-ischemic brain injury in the neonatal rat. J Neurosci Res 56: 60–71.
14. Ong WY, Ling SF, Yeo JF, Chiueh CC, Farooqui AA (2005) Injury and recovery of pyramidal neurons in the rat hippocampus after a single episode of oxidative stress induced by intracerebroventricular injection of ferrous ammonium citrate. Reprod Nutr Dev 45: 647–662.
15. Horky LL, Pluta RM, Boock RJ, Oldfield EH (1998) Role of ferrous iron chelator 2,2′-dipyridyl in preventing delayed vasospasm in a primate model of subarachnoid hemorrhage. J Neurosurg 88: 298–303.
16. Rauhala P, Khaldi A, Mohanakumar KP, Chiueh CC (1998) Apparent role of hydroxyl radicals in oxidative brain injury induced by sodium nitroprusside. Free Radic Biol Med 24: 1065–1073.
17. Young HM, O'Brien AJ, Furness JB, Ciampoli D, Hardwick JP, et al. (1997) Relationships between NADPH diaphorase staining and neuronal, endothelial, and inducible nitric oxide synthase and cytochrome P450 reductase immunoreactivities in guinea-pig tissues. Histochem Cell Biol 107: 19–29.
18. Zhen J, Lu H, Wang XQ, Vaziri ND, Zhou XJ (2008) Upregulation of endothelial and inducible nitric oxide synthase expression by reactive oxygen species. Am J Hypertens 21: 28–34.
19. del Zoppo G, Ginis I, Hallenbeck JM, Iadecola C, Wang X, et al. (2000) Inflammation and stroke: putative role for cytokines, adhesion molecules and iNOS in brain response to ischemia. Brain Pathol 10: 95–112.
20. Lopez-Ongil S, Hernandez-Perera O, Navarro-Antolin J, Perez de Lema G., Rodriguez-Puyol M, et al. (1998) Role of reactive oxygen species in the signalling cascade of cyclosporine A-mediated up-regulation of eNOS in vascular endothelial cells. Br J Pharmacol 124: 447–454.
21. Shih HC, Lin CL, Lee TY, Lee WS, Hsu C (2006) 17beta-Estradiol inhibits subarachnoid hemorrhage-induced inducible nitric oxide synthase gene expression by interfering with the nuclear factor kappa B transactivation. Stroke 37: 3025–3031.
22. Lin CL, Shih HC, Dumont AS, Kassell NF, Lieu AS, et al. (2006) The effect of 17beta-estradiol in attenuating experimental subarachnoid hemorrhage-induced cerebral vasospasm. J Neurosurg 104: 298–304.
23. Xu J, He L, Ahmed SH, Chen SW, Goldberg MP, et al. (2000) Oxygen-glucose deprivation induces inducible nitric oxide synthase and nitrotyrosine expression in cerebral endothelial cells. Stroke 31: 1744–1751.
24. Mohanakumar KP, de Bartolomeis A, Wu RM, Yeh KJ, Sternberger LM, et al. (1994) Ferrous-citrate complex and nigral degeneration: evidence for free-radical formation and lipid peroxidation. Ann N Y Acad Sci 738: 392–399.
25. West KA, Brognard J, Clark AS, Linnoila IR, Yang X, et al. (2003) Rapid Akt activation by nicotine and a tobacco carcinogen modulates the phenotype of normal human airway epithelial cells. J Clin Invest 111: 81–90.
26. Chen LC, Liu YC, Liang YC, Ho YS, Lee WS (2009) Magnolol inhibits human glioblastoma cell proliferation through upregulation of p21/Cip1. J Agric Food Chem 57: 7331–7337.
27. Ho PY, Zhong WB, Ho YS, Lee WS (2006) Terbinafine inhibits endothelial cell migration through suppression of the Rho-mediated pathway. Mol Cancer Ther 5: 3130–3138.
28. Wilkinson DS, Ogden S K, Stratton SA, Piechan JL, Nguyen TT, et al. (2005) A direct intersection between p53 and transforming growth factor beta pathways targets chromatin modification and transcription repression of the alpha-fetoprotein gene. Molecular and cellular biology 25: 1200–1212.
29. Gaasch JA, Lockman PR, Geldenhuys WJ, Allen DD, Van der Schyf CJ (2007) Brain iron toxicity: differential responses of astrocytes, neurons, and endothelial cells. Neurochem Res 32: 1196–1208.
30. Won SM, Lee JH, Park UJ, Gwag J, Gwag BJ, et al. (2011) Iron mediates endothelial cell damage and blood-brain barrier opening in the hippocampus after transient forebrain ischemia in rats. Exp Mol Med 43: 121–128.
31. Otani H (2009) The role of nitric oxide in myocardial repair and remodeling. Antioxid Redox Signal 11: 1913–1928.
32. Qi WN, Chaiyakit P, Cai Y, Allen DM, Chen LE, et al. (2004) NF-kappaB p65 involves in reperfusion injury and iNOS gene regulation in skeletal muscle. Microsurgery 24: 316–323.
33. Van Bergen P, Rauhala P, Spooner CM, Chiueh CC (1999) Hemoglobin and iron-evoked oxidative stress in the brain: protection by bile pigments, manganese and S-nitrosoglutathione. Free Radic Res 31: 631–640.
34. Chiueh CC, Andoh T, Lai AR, Lai E, Krishna G (2000) Neuroprotective strategies in Parkinson's disease: protection against progressive nigral damage induced by free radicals. Neurotox Res 2: 293–310.
35. Janjua N, Mayer SA (2003) Cerebral vasospasm after subarachnoid hemorrhage. Curr Opin Crit Care 9: 113–119.
36. Amberg G.C, Earley S, Glapa SA (2010) Local regulation of arterial L-type calcium channels by reactive oxygen species. Circ Res 107: 1002–1010.
37. Du W, Frazier M, McMahon TJ, Eu JP (2005) Redox activation of intracellular calcium release channels (ryanodine receptors) in the sustained phase of hypoxia-induced pulmonary vasoconstriction. Chest 128: 556S–558S.

38. Berra LV, Carcereri De Prati A, Suzuki H, Pasqualin A (2007) The role of constitutive and inducible nitric oxide synthase in the human brain after subarachnoid hemorrhage. J Neurosurg Sci 51: 1–9.
39. Hanggi D, Steiger HJ (2006) Nitric oxide in subarachnoid haemorrhage and its therapeutics implications. Acta Neurochir (Wien) 148: 605–613; discussion 613.
40. Vijay A, Santhanam R, Katusic ZS (2006) Genetic modification of cerebral arterial wall: implications for prevention and treatment of cerebral vasospasm. Neurol Res 28: 759–768.
41. Aladag MA, Turkoz Y, Parlakpinar H, Ozen H, Egri M, et al. (2009) Melatonin Ameliorates Cerebral Vasospasm After Experimental Subarachnoidal Haemorrhage Correcting Imbalance of Nitric Oxide Levels in Rats. Neurochem Res 34: 1935–1944.
42. Osuka K, Watanabe Y, Usuda N, Atsuzawa K, Yoshida J, et al. (2009) Modification of Endothelial Nitric Oxide Synthase through AMPK after Experimental Subarachnoid Hemorrhage. J Neurotrauma 26: 1157–1165.
43. Ayer RE, Zhang JH (2008) Oxidative stress in subarachnoid haemorrhage: significance in acute brain injury and vasospasm. Acta Neurochir Suppl 104: 33–41.
44. Regunathan S, Piletz JE (2003) Regulation of inducible nitric oxide synthase and agmatine synthesis in macrophages and astrocytes. Ann N Y Acad Sci 1009: 20–29.
45. Morris SM Jr, Billiar TR (1994) New insights into the regulation of inducible nitric oxide synthesis. Am J Physiol 266: E829–839.
46. Wong JM, Billiar TR (1995) Regulation and function of inducible nitric oxide synthase during sepsis and acute inflammation. Adv Pharmacol 34: 155–170.
47. Taylor BS, Geller DA (2001) Regulation of the inducible Nitric Oxide Synthase gene. In: Salvemini, O.; Billiar, T.R.; Vodovotz, Y., eds. Nitric Oxide & inflammation,. basel; Boston; Berlin; Birkhauser; 1–26.
48. Taylor BS, Geller DA (2000) Molecular regulation of the human inducible nitric oxide synthase (iNOS) gene. Shock 13: 413–424.
49. Ortego M, Gómez-Hernández A, Vidal C, Sánchez-Galán E, Blanco-Colio LM, et al. (2005) HMG-CoA reductase inhibitors reduce I kappa B kinase activity induced by oxidative stress in monocytes and vascular smooth muscle cells. J Cardiovasc Pharmacol 45: 468–475.
50. Jaramillo M, Gowda DC, Radzioch D, Olivier M (2003) Hemozoin increases IFN-γ-inducible macrophage nitric oxide generation through extracellular signal-regulated kinase- and NFκB-dependent pathways. J Immunol 171: 4243–4253.
51. Asehnoune K, Strassheim D, Mitra S, Kim JY, Abraham E (2004) Involvement of reactive oxygen species in toll-like receptor 4-dependent activation of NFκB. J Immunol 172: 2522–2529.

出席國際學術會議心得報告

計畫編號	99-2320-B-037-024-MY3
計畫名稱	NSC 101-2629-B-037 -001 -
出國人員姓名 服務機關及職稱	李文森 台北醫學大學醫學院 醫學科學研究所 教授
會議時間地點	11~14, Apr, 2013, Istanbul, Turkey
會議名稱	The 7th World Congress on Controversies in Neurology (CONy)
發表論文題目	**Estrogen-induced decreases of ferrous citrate complex-induced NOS2 upregulation in cerebral endothelial cells**

一、 參加會議經過

The World Congress on Controversies in Neurology (CONy)為每年舉辦之神經科學最新相關研究，研討會之重點為神經科學方面較具爭論性的議題。本次會議於四月11-14號在土耳其伊斯坦堡舉行，由**Murat Emre**及**Amos D. Korczyn**共同籌劃舉辦。今年總計有來自全球多個國家超過1000名人士參與此次會議。大會共邀請五十位學者專家進行學術演講並有近1200篇壁報論文發表。演講及論文發表內容涵蓋Stroke，Auto-immune diseases，Parkinson's disease，Dementia & Alzheimer's disease，Epilepsy，Headache & Pain，Multiple Sclerosis，Perpheral Neuropathy，Rehabilitation等領域。講者皆為來自世界各地該領域之專家學者。演講內容非常豐富，學者間的交流熱烈，收穫良多。

個人在4月14日在以" **Estrogen-induced decreases of ferrous citrate complex-induced NOS2 upregulation in cerebral endothelial cells**"為主題的e-poster發表，這是較特殊的方式，海報之檔案已於日前上傳至大會，而報告當天每個海報的報告人皆須上台做口頭報告，並進行Q&A。過程中與多位研究領域相近的學者共同切磋討論。大會亦邀請知名廠商與藥廠於會場附設展示攤位。大會用心將議程以研究主題做劃分，讓與會者可快速搜尋有興趣的演講也提供相同領域研究者更多相互切磋的機會。

二、 與會心得

近年來，生物醫學之研究進展十分神速，參加國際研討會是獲得新知的一個很好的方法。除了可以了解目前研究的趨勢外，也可以與相同領域的國際學者們互相切磋。本次會議演講議題及論文報告包含有與神經科學相關的基礎醫學與臨床醫學研究，藉此機會國際

學者互相交換研究的經歷與心得。觀看了來自世界各地學者的演講及壁報論文報告，一方面體驗到現今研究確實需要團隊合作/跨領域研究的模式，另一方面在研究方法的日新月異及實驗設計上的嚴謹度及邏輯思考方面亦有很多的學習心得，深感參與此次會議 對於未來在研究設計與論文發表等各方面皆獲得相當寶貴的經驗。此外，會議地點安排在大飯店中，使與會人士能以更輕鬆的方式來進行學術研討，著實有著極佳的效果。

三、 其他 (附上參與學會及海報論文展示之照片)

上台做口頭報告 (12th, Apr. 2013. Istanbul, Turkey)

海報論文展示:

Wen-Sen Lee, Li-Ching Chen, Chin Hsu. "**Estrogen-induced decreases of ferrous citrate complex-induced NOS2 upregulation in cerebral endothelial cells".** The 7th World Congress on Controversies in Neurology (CONy). Istanbul, Turkey. 11~14, Apr, 2013.

國科會補助計畫衍生研發成果推廣資料表

日期:2013/10/18

國科會補助計畫	計畫名稱: 以性別特異性神經保護策略治療出血性腦損傷 - 整合分子與治療解決臨床疾病 (GM03)
	計畫主持人: 許勤
	計畫編號: 101-2629-B-037-001- 學門領域: 性別主流科技計畫

無研發成果推廣資料

101 年度專題研究計畫研究成果彙整表

計畫主持人：許勤	計畫編號：101-2629-B-037-001-
計畫名稱：以性別特異性神經保護策略治療出血性腦損傷 - 整合分子與治療解決臨床疾病（GM03)--以性別特異性神經保護策略治療出血性腦損傷 - 整合分子與治療解決臨床疾病（GM03）	

成果項目			量化			單位	備註（質化說明：如數個計畫共同成果、成果列為該期刊之封面故事...等）
			實際已達成數（被接受或已發表）	預期總達成數(含實際已達成數)	本計畫實際貢獻百分比		
國內	論文著作	期刊論文	0	0	100%	篇	
		研究報告/技術報告	0	0	100%		
		研討會論文	0	0	100%		
		專書	0	0	100%		
	專利	申請中件數	0	0	100%	件	
		已獲得件數	0	0	100%		
	技術移轉	件數	0	0	100%	件	
		權利金	0	0	100%	千元	
	參與計畫人力（本國籍）	碩士生	0	0	100%	人次	
		博士生	0	0	100%		
		博士後研究員	0	0	100%		
		專任助理	0	0	100%		
國外	論文著作	期刊論文	3	3	100%	篇	1.Li-Ching Chen, Chin Hsu, Chuang Chin Chiueh, Wen-Sen Lee (2012): Ferrous citrate up-regulates the NOS2 through nuclear translocation of NFκB induced by free radicals generation in mouse cerebral endothelial cells. PLoS ONE 7(9): e46239. 2 Guo-Jing Cheng

							iron oxide nanoparticles as a nanotheranostic agent for brain glioma.(Submitted) 3.Sex dimorphic role of HO-1 in iron-induced striatal injury and the neuroprotection conferred by estradiol.(in preparation)
		研究報告/技術報告	0	0	100%		
		研討會論文	0	0	100%		
		專書	0	0	100%	章/本	
	專利	申請中件數	0	0	100%	件	
		已獲得件數	0	0	100%		
	技術移轉	件數	0	0	100%	件	
		權利金	0	0	100%	千元	
	參與計畫人力（外國籍）	碩士生	0	0	100%	人次	
		博士生	0	0	100%		
		博士後研究員	0	0	100%		
		專任助理	1	1	100%		
其他成果 (無法以量化表達之成果如辦理學術活動、獲得獎項、重要國際合作、研究成果國際影響力及其他協助產業技術發展之具體效益事項等，請以文字敘述填列。)		無					

	成果項目	量化	名稱或內容性質簡述
科教處計畫加填項	測驗工具(含質性與量性)	0	
	課程/模組	0	
	電腦及網路系統或工具	0	
	教材	0	
	舉辦之活動/競賽	0	
	研討會/工作坊	0	
	電子報、網站	0	

目	計畫成果推廣之參與（閱聽）人數	0	

國科會補助專題研究計畫成果報告自評表

請就研究內容與原計畫相符程度、達成預期目標情況、研究成果之學術或應用價值（簡要敘述成果所代表之意義、價值、影響或進一步發展之可能性）、是否適合在學術期刊發表或申請專利、主要發現或其他有關價值等，作一綜合評估。

1. 請就研究內容與原計畫相符程度、達成預期目標情況作一綜合評估

■達成目標

□未達成目標（請說明，以 100 字為限）

□實驗失敗

□因故實驗中斷

□其他原因

說明：

2. 研究成果在學術期刊發表或申請專利等情形：

論文：■已發表 □未發表之文稿 □撰寫中 □無

專利：□已獲得 □申請中 ■無

技轉：□已技轉 □洽談中 ■無

其他：（以 100 字為限）

已發表論文 1 篇

投稿中論文 1 篇

撰寫中論文 1 篇

3. 請依學術成就、技術創新、社會影響等方面，評估研究成果之學術或應用價值（簡要敘述成果所代表之意義、價值、影響或進一步發展之可能性）（以 500 字為限）

血氧基質-1(heme oxygenase-1； HO-1)在檸檬酸亞鐵引起尾狀核損傷扮演著性別差異性的角色，即雄鼠 HO-1 減少時檸檬酸亞鐵引起的腦損傷嚴重度較為輕微。本研究結果開啟性別特異性治療的前景，臨床上可針對顱內出血導致較嚴重急性鐵離子過度釋放之男性病患，以減少 HO-1 之誘發性做為預防腦損傷嚴重度之策略。